

GATOS N: The first direct kinematic evidence of dusty outflows from AGN via PAH kinematics of local Seyfert galaxies with JWST

Fergus R. Donnan,^{1,2*} Ismael García-Bernete,³ Dimitra Rigopoulou,^{1,4} Almudena Alonso-Herrero,³ Anelise Audibert,^{5,6} Enrica Bellocchi,^{7,8} Andrew Bunker,¹ Steph Campbell,⁹ Françoise Combes,¹⁰ Richard Davies,¹¹ Tanio Díaz-Santos,¹² Juan A. Fernández-Ontiveros,¹³ Poshak Gandhi,¹⁴ Santiago García-Burillo,¹⁵ O. González-Martín,¹⁶ Erin K. S. Hicks,¹⁷ Laura Hermosa Muñoz,³ Sebastian F. Hoenig,¹⁴ Masatoshi Imanishi,^{18,19} Alvaro Labiano,²⁰ Nancy A. Levenson,²¹ Miguel Pereira-Santaella,²² Cristina Ramos Almeida,^{5,6} Claudio Ricci,^{23,24} Rogemar A. Riffel,²⁵ Daniel Rouan,²⁶ David Rosario,⁹ Karin Sandstrom,² T. Taro Shimizu,¹¹ Marko Stalevski,^{27,28} Niranjana Thatte,¹ Oscar Veenema,¹ Lulu Zhang,²⁹

(Affiliations can be found after the references)

Accepted XXX. Received YYY; in original form ZZZ

ABSTRACT

We present the first spatially resolved kinematic evidence for dust in the outflows of Active Galactic Nuclei (AGN). We utilise observations from JWST with NIRSpec IFU and MIRI MRS data of 10 local Seyferts and use Principal Component Analysis (PCA) tomography to extract the kinematics of Polycyclic Aromatic Hydrocarbon (PAH) features. PAHs comprise the smallest carbonaceous dust molecules in the Interstellar Medium (ISM), and produce emission features in the infrared providing the potential to measure kinematics. This is however challenging due to their broad shapes and variations in their intrinsic profile, prompting the need for techniques such as PCA tomography. We find that the velocity of the PAHs is similar to the molecular gas as traced by the rotational transitions of H₂, where for NGC 5728 and NGC 7582, both disk and outflow are present. We detect the outflow in the kinematics of large and neutral PAHs, namely the 11.3 μm and 17 μm PAH features, where after subtracting the disk, the velocity field matches that of high-ionisation potential lines such as [NeVI] (7.65 μm, IP = 158 eV). Finally, we fail to detect kinematics of the 6.2 μm PAH due to an altered intrinsic profile while the 3.3 μm PAH kinematics purely trace the circumnuclear disk. This suggests the PAHs in the outflow are more neutral and larger than in star-forming regions, consistent with PAH band ratios in previous studies of AGN.

Key words: galaxies: kinematics and dynamics – galaxies: ISM – techniques: spectroscopic

1 INTRODUCTION

Active Galactic Nuclei (AGN), powered by accretion onto a super-massive black hole (SMBH), are known to play a key role in the evolution of galaxies (e.g. Kormendy & Ho 2013; Heckman & Best 2014), where vast quantities of energy are radiatively and kinematically ejected into the host galaxy (e.g., Silk & Rees 1998; Fabian 2012; Combes 2017).

The idea that AGN are dynamic and evolving systems that interact with the host galaxy, suggests that the early model of a static torus (Antonucci & Miller 1985; Antonucci 1993), to explain the presence or lack of presence of broad emission lines on AGN spectra, does not tell the full picture. More contemporary models (See Ramos Almeida & Ricci 2017; Hönig 2019, for recent reviews.) feature clumpy or two-phase media, with polar and toroidal dust (e.g. Nenkova et al.

2008a,b; Hönig & Kishimoto 2010, 2017; Stalevski et al. 2016) or that the torus itself is the result of a failed wind (Wada 2012).

The existence of dust in the polar direction, perpendicular to the torus, has long been postulated from ground based imaging (Braatz et al. 1993; Bock et al. 2000; Radomski et al. 2002, 2008; Packham et al. 2005; Reunanen et al. 2010; Asmus et al. 2014, 2016; Asmus 2019; Stalevski et al. 2017) but particularly with the advent of interferometry in the infrared revealing polar structure (Raban et al. 2009; Hönig et al. 2012, 2013; López-Gonzaga et al. 2014; Tristram et al. 2014; López-Gonzaga et al. 2016; Leftley et al. 2018; Isbell et al. 2022; Gámez Rosas et al. 2022). Interferometry probes dust on very small scales, comparable to the torus itself (~ 10s pc García-Burillo et al. 2019, 2021; Combes et al. 2019; Alonso-Herrero et al. 2021) and are thought to be dust driven from the inner regions of the torus by an AGN wind, alongside the molecular and ionised phases of the outflow. Larger scale dusty structures have also been detected with JWST/MIRI imaging after carefully removing contamination from

* E-mail: fdonnan@ucsd.edu

emission lines (Haidar et al. 2024; Campbell et al. 2025; Haidar et al. 2026). It is unclear however if this dust is simply heated by the AGN or actually launched by the AGN. Indeed Haidar et al. (2026) suggests AGN radiation alone is not sufficient to heat the dust and that shocks may play a role. Moreover, AGN outflows can entrain material from the host galaxy (e.g. García-Bernete et al. 2021), which may be necessary to launch dusty outflows. A key missing diagnostic of this dust, unlike the gas phase, are its kinematics.

Polycyclic Aromatic Hydrocarbons (PAHs) comprise the smallest carbonaceous dust molecules and consist of rings of carbon bonded with hydrogen. These molecules are radiatively excited by UV photons from young stars, where the subsequent de-excitation via the stretching and bending of C-C and C-H bonds results in a suite of broad emission features in the infrared (3-17 μm) (e.g. Tielens 2008; Li 2020). While graphite and silicate dust grains produce a continuum that is unsuitable to measuring kinematics, the emission profiles of PAH molecules provide the possibility of measuring kinematics, but their broad shapes provide significant challenges (Donnan et al. 2024).

Unlike in star-forming regions, PAHs exhibit low equivalent widths (EW) in AGN due to the strong infrared continuum in such sources but also destruction of PAH molecules from the AGN radiation field (e.g. Rapacioli et al. 2006; Schweitzer et al. 2006; Alonso-Herrero et al. 2014) or shocks (e.g. Micelotta et al. 2010). Recent studies, taking advantage of the increased sensitivity and spatial resolution of JWST, have found that PAHs survive in the vicinity of AGN and in their outflows (García-Bernete et al. 2022a,b; Lai et al. 2023; García-Bernete et al. 2024; Rigopoulou et al. 2024; Zhang et al. 2024b; Donnelly et al. 2024; Ramos Almeida et al. 2025b). However, their properties appear to be altered, where neutral PAHs appear to survive while AGN have less ionised PAHs potentially suggesting preferential destruction of ionised PAHs. It is unclear however whether these PAHs are travelling within the AGN outflow itself or are simply residing in star-forming regions that are impacted by the outflow where the PAH properties become altered. To answer this question requires a kinematic analysis of the PAH features.

Measuring the kinematics of PAH features is challenging for two main reasons. Firstly, they are significantly broader than any Doppler shift in wavelength due to the velocity of the PAH molecules. Secondly, the intrinsic shape of the feature is not well defined, often appearing asymmetric, containing broad wings akin to a Lorentzian or Drude profile rather than a Gaussian. Moreover the profile can change depending on the properties of the PAH population such as charge, size and the hardness of the radiation field (e.g. Peeters et al. 2002; Candian & Sarre 2015; Shannon & Boersma 2019). This makes it difficult to establish the rest-frame emission to provide a reference to measure any deviations due to the velocity field of the PAHs.

To overcome the above issues, Donnan et al. (2024) presented the first use of the technique of Principal Component Analysis (PCA) tomography to detect the signature of kinematics of the 3.3 μm PAH in three local LIRGs. The technique of PCA tomography was first presented in Steiner et al. (2009). PCA tomography, when applied to a data cube containing a PAH feature, can detect the spectral signature of a blue/red shifted feature, using the information held within the spatial axes. This allows one to construct a velocity map of these features without modelling the spectra of each spaxel.

In this work we apply PCA tomography to a sample of nearby Seyfert galaxies, observed with JWST/MIRI MRS and JWST/NIRSpec IFU, to measure the dust kinematics and compare with other phases of the ISM. All the Seyfert galaxies host both AGN-driven outflows and ongoing star formation which makes them

ideal targets to study the potential dust phase of AGN outflows and their impact on their host galaxy. The paper is laid out as follows. In Section 2, we describe the sample and the observations with JWST. In Section 3, we describe the method of PCA tomography. In Section 4 we present velocity maps for each target. Finally, in Section 5 we discuss our results. Throughout this work we assume ΛCDM cosmology with $H_0 = 70 \text{ km s}^{-1} \text{ Mpc}^{-1}$, $\Omega_m = 0.27$, $\Omega_\Lambda = 0.73$.

2 OBSERVATIONS AND DATA REDUCTION

In this work we use 10 local Seyfert galaxies as part of the GATOS (Galaxy Activity Torus and Outflow Survey) sample observed with both MIRI MRS and NIRSpec IFU providing spatially resolved spectroscopy from $\sim 3\mu\text{m} - 28\mu\text{m}$. A summary of the physical properties of these targets are shown in Table 1. The data are compiled from four JWST General Observer programs over cycles 1, 2, and 3. These are GO 1670 (P.I. T. Shimizu), GO 3535 (P.I. I. Garcia-Bernete & D. Rigopoulou), GO 5017 (P.I. I. Garcia-Bernete & A. Alonso-Herrero & D. Rigopoulou), and GO 1875 (P.I. J. Fernandez Ontiveros).

All of the targets contain outflows clearly detected in the ionised phase (e.g. Davies et al. 2020) as well as star-formation in the circum-nuclear regions which have strong PAH emission, although some targets are much more dominated by the nuclear emission such as MCG-05-23-016 (e.g. González-Martín et al. 2025; Esparza-Arredondo et al. 2025).

We primarily followed the standard pipeline procedure (e.g., Labiano et al. 2016 and references therein) and the same configuration of the pipeline stages described in García-Bernete et al. (2022b) and Pereira-Santaella et al. (2022) to reduce the data. Some hot and cold pixels are not identified by the current pipeline, so we added some extra steps, as is described in Pereira-Santaella et al. (2024) and García-Bernete et al. (2024) for NIRSpec and MRS, respectively. We used calibration version 1.18.1 with CDRS version 12.1.4 for the data reduction.

Both the MIRI and NIRSpec cubes are produced in the IFU alignment, where the spatial axes are aligned with the position angle of the telescope when the observations were taken. Any analysis is performed on the cubes in the IFU alignment before being rotated into the sky orientation (north is up, east is left) only when plotting. This reduces any further errors that may be introduced when reprojecting the data.

3 PCA TOMOGRAPHY

The technique of PCA tomography was first presented in Steiner et al. (2009) and applied to JWST data in Donnan et al. (2024) to reveal the kinematics of PAH features for the first time. We summarise the technique below before demonstrating the technique in Fig. 1.

The purpose of PCA is to reorder the data into principal components which contain a decreasing fraction of the total information held within the data. These components are linear, meaning the original data can be reconstructed by summing the principal components. When applied to data cubes containing two spatial dimensions and one spectral dimension, each principal component contains a specific spectral feature that has some distribution in the spatial dimensions.

Before applying the PCA decomposition, the cubes are prepared in the following way. First the spectral feature of interest is isolated in wavelength, creating a sub-cube. A local continuum is then fit assuming a simple straight line before it being subtracted. The resulting

Table 1. Summary of Targets

Name	RA	Dec	z	Observing Program	$\log L_{\text{bol}}$ (erg s^{-1})	$\log \lambda_{\text{Edd}}$	$\log M_{\text{BH}}$ (M_{\odot})	Disk PA	Outflow PA	Ref.
ESO 420-G013	04h13m49.6804s	-32d00m25.153s	0.012	GO 5017, GO 1875	-	-	-	230°	32°	(1)
MCG-05-23-016	09h34m06.3120s	+27d20m59.402s	0.042	GO 5017, GO 1670	44.3	-1.70	7.9	246°	172°	(2),(3),(4),(5)
NGC 3081	09h59m29.5431s	-22d49m34.720s	0.008	GO 1670, GO 5017	44.1	-1.20	7.20	90°	180°	(6),(4),(7)
NGC 3227	10h23m30.5748s	+19d51m54.340s	0.004	GO 3535	43.3	-1.84	7.04	332°	30°	(8),(9),(10),(11)
NGC 4051	12h03m09.6073s	+44d31m52.709s	0.002	GO 3535	42.4	-1.94	6.24	50°	80°	(9),(12)
NGC 5506	14h13m14.8756s	-03d12m27.698s	0.006	GO 1670	44.1	-1.30	7.3	271°	22°	(9),(13),(4)
NGC 5728	14h42m23.8735s	-17d15m10.855s	0.009	GO 5017, GO 1670	44.1	-1.53	7.53	14°	293°	(14),(15),(16)
ESO 137-G034	16h35m14.0026s	-58d04m47.869s	0.009	GO 1670, GO 5017	43.4	-2.10	7.4	348°	304°	(3),(4),(17)
NGC 7172	22h02m01.8945s	-31d52m10.525s	0.009	GO 1670	44.1	-2.30	8.3	90°	0°	(18),(4),(19)
NGC 7582	23h18m23.6280s	-42d22m13.512s	0.005	GO 3535	43.3	-1.42	6.62	168°	221°	(20),(21)

Observing Programs: GO 1670 (P.I. T. Shimizu), GO 3535 (P.I. I. Garcia-Bernete & D. Rigopoulou), GO 5017 (P.I. I. Garcia-Bernete, A. Alonso-Herrero, D. Rigopoulou), GO 1875 (P.I. J. Fernandez Ontiveros).

Both the disk and outflow position angles are measured east of north to the blueshifted side.

References numbered by first appearance in the table: (1) (Fernández-Ontiveros et al. 2020) (2) (Esparza-Arredondo et al. 2025) (3) (Zhang et al. 2024a) (4) (Davies et al. 2020) (5) (Ponti et al. 2012) (6) (Schnorr-Müller et al. 2016) (7) (Gliozzi et al. 2024) (8) (Alonso-Herrero et al. 2019) (9) (Fischer et al. 2013) (10) (Bentz et al. 2023) (11) (Mehdipour et al. 2021) (12) (Denney et al. 2009) (13) (Gofford et al. 2015) (14) (Shimizu et al. 2019) (15) (Davies et al. 2015) (16) (Durré & Mould 2018) (17) (Caglar et al. 2020) (18) (Alonso Herrero et al. 2023) (19) (Smajić et al. 2012) (20) (Veenema & et al. submitted 2026) (21) (Poitevineau et al. 2025)

cube has the form $\mathbf{I}_{x,y,\lambda}$ which is then collapsed into two dimensions where the spatial dimensions, x, y are transformed by

$$\beta = \mu(x - 1) + y. \quad (1)$$

resulting in a cube, $\mathbf{I}_{\beta,\lambda}$. The PCA is applied to this cube where

$$\mathbf{T}_{\beta,k} = \mathbf{I}_{\beta,\lambda} \cdot \mathbf{E}_{\lambda,k}, \quad (2)$$

where $\mathbf{T}_{\beta,k}$ are the tomograms of each principal component, k , which describes the spatial distribution of a given spectral feature, $\mathbf{E}_{\lambda,k}$, which are known as eigenspectra. We additionally mask low signal to noise spaxels as this can “confuse” the PCA as it treats each spaxel with equal weight. We measure the signal to noise by first measuring the noise by smoothing the spectrum of each spaxel (in the case of a PAH feature) and subtracting from the data. The noise is then measured as the standard deviation of the residuals. In the case of an emission line, we mask the line and measure the standard deviation. The signal to noise is then the peak flux of the feature over the noise. We mask spaxels with a signal to noise ratio < 5 . We additionally smooth each channel of the data cube with a Gaussian kernel with $\sigma = 1$ pixel to improve the signal to noise before masking. For the 17 μm PAH, we increase the smoothing to 2 pixels as well as lowering the signal to noise mask to < 1 , as the data is significantly noisier for this particular feature. The 17 μm PAH is comprised of several sub-bands however we only use the 16.4 μm sub feature to measure the kinematics of the 17 μm PAH, as the full feature is extremely broad while the 16.4 μm sub feature is relatively narrow.

Additionally for the 3.3 μm PAH and the 6.2 μm PAH, we mask emission lines that are blended with the feature. In particular at 3.296 μm the H I 9-5 line is masked as well as the H₂ S(6) line at 6.109 μm .

We demonstrate the PCA technique applied to the 3.3 μm PAH for NGC 7582 in Fig. 1, where we show the first four principal components. From the PCA decomposition it is clear that the first principal component describes the rest frame emission of the feature, where

the eigenspectrum shows the restframe profile while the tomogram shows the emission map. The second principal component contains kinematic information, where the eigenspectrum shows a lack of emission on the blue side but an increase in emission on the red side, corresponding to a redshifted profile. Where the second tomogram is positive, the feature is redshifted and where the tomogram is negative the feature is blueshifted. The higher order components contain progressively less information, eventually only containing noise. In Fig. 1, the third and fourth components may contain additional velocity information and/or small differences in the intrinsic profile. Considering the third tomogram is similar to the second, it likely contains additional velocity information, however the fourth tomogram is not particularly clear and may just be noise. As we will show in section 5.2, in the case 6.2 μm PAH, small differences in the intrinsic profile are present instead of kinematics. The tomogram is powerful for distinguishing between kinematics and variations in the intrinsic profile as it can be compared to known line kinematics. When variations in the intrinsic profile do show up, it is clear from the tomogram, which is indeed the case for the 6.2 μm PAH which we discuss in section 5.2. We find that the 3.3 μm , 11.3 μm and 17 μm PAHs all show kinematics rather than differences in the intrinsic profile.

To construct a velocity map from the principal components, we take the first principal component as the rest frame emission over the field of view. The eigenspectrum for this component is then used as a reference to measure the velocity for each spaxel. We do this by reconstructing the original cube using the first 4 components (subsequent components contain $\lesssim 1\%$ of the variance (Donnan et al. 2024)) and then measuring the velocity offset between the spectrum of a given spaxel and the eigenspectrum of the first principal component. The velocity of a spaxel is given by

$$V_{x,y} = 3 \times 10^5 \Delta\lambda_{x,y} / \lambda_0 \text{ km s}^{-1}, \quad (3)$$

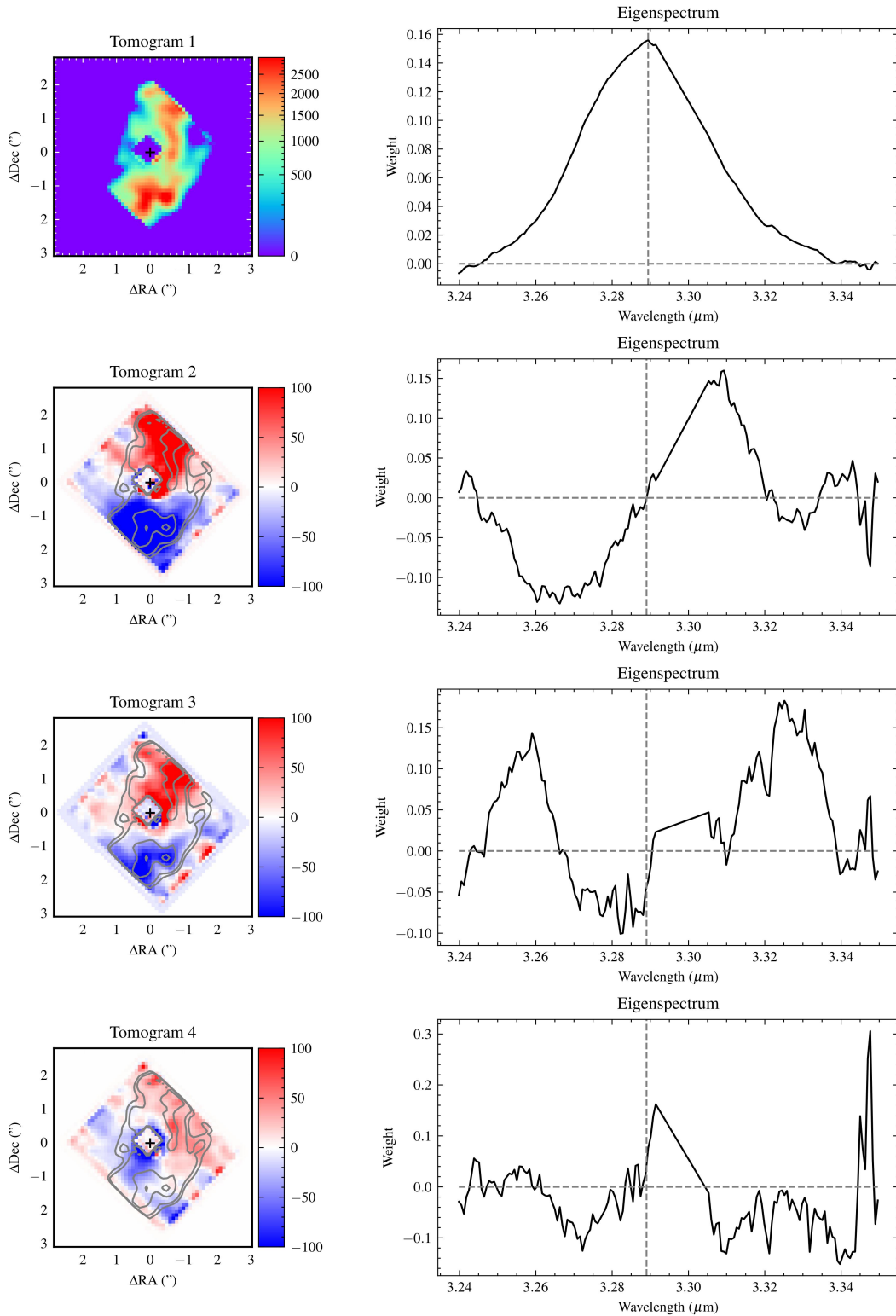


Figure 1. The first four principal components of the $3.3 \mu\text{m}$ PAH for NGC 7582. Each row shows each component, where the higher components contain progressively less information held within the original data cube. The left panels show the tomograms which show the spatial distribution of the eigenspectra in the right panels. The first component describes the rest frame emission of the feature while the second component shows a redshifted/blueshifted feature on either side of the nucleus, indicative of rotation. The higher order components contain extra information on the velocity field and/or variations in the intrinsic profile of the PAH feature. The contours overlaid on the tomograms show the first principal component. Note that the colour scale for each of the tomograms is not velocity but rather a correlation coefficient of how strongly each eigenspectrum maps onto the spatial dimensions. The vertical dashed grey lines show the wavelength where the second eigenspectrum crosses zero, showing the kinematic centre. Note that the smooth line between $3.29 - 3.30 \mu\text{m}$ that can be seen in the Eigenspectra is due to the masking of the Pf δ line.

where $\Delta\lambda_{x,y}$ is the shift measured between the first principal component and each spaxel of the reconstructed data cube using the first 4 principal components. λ_0 is the reference wavelength, which in the case of an emission line is just the rest wavelength of the feature. For the PAH features, there is no clear reference wavelength due to the intrinsic broadness and asymmetry of the profile. We therefore use the wavelength where the second principal component (which contains the majority of the kinematic information) crosses from positive to negative as demonstrated in Fig. 1. This point represents the kinematic centre, making it a good measure of λ_0 .

Donnan et al. (2024) demonstrated that this technique is effective in recovering the velocity field as compared to more traditional methods. The necessity to use PCA tomography to measure the velocity field of PAH features over more traditional methods such as fitting each spaxel, results from two major advantages it has over simple velocity cross-correlation. First, the PCA can detect shifts in the rest-frame feature, using all the information contained within the spatial dimensions, picking out the signature of kinematics. Secondly, there is not well defined a priori restframe profile for PAH features and so the first principal component provides a reference profile to be able to measure the velocity field.

4 RESULTS

4.1 Velocity Maps

We run the PCA analysis for each target for a variety of spectral features, probing different phases of the ISM. To clearly isolate the outflow we use the [NeVI] (7.65 μm), which has an ionisation potential of 158 eV making it an unambiguous tracer of AGN photoionisation (e.g. Sturm et al. 2002).

We then probe the molecular gas using the rotational transitions of H_2 , where we use the S(5) (6.91 μm) to probe the hot molecular gas and the S(1) (17.03 μm) to probe the cooler molecular gas. As Davies et al. (2024) demonstrated, if the outflow is detected in the molecular phase, the hotter H_2 transitions trace more of the outflow than the cooler transitions, where CO (2-1), probing even cooler molecular gas, shows no detection in the outflow (Shimizu et al. 2019). It is worth noting however that the relatively low FOV of MIRI means we may miss molecular outflows on very large scales (\gtrsim kpc).

We extract the kinematics of the PAH features, providing a probe of the dust phase and in particular small carbonaceous dust. We focus on the 3.3 μm , 11.3 μm and 17.0 μm (via the 16.4 μm sub-feature) features due to their relative lack of blending with other features. We note that the results using the 6.2 μm PAH feature do not easily compare with what we see from the other features. This might be because the 6.2 μm PAH feature arises from ionised PAHs which could be subject to destruction by the radiation field of the AGN (e.g. García-Bernete et al. 2024), leading to a relatively low signal to noise in outflow regions compared to other PAH features. The PCA appears to select different intrinsic profiles for the outflow regions compared to SF regions for the 6.2 μm feature. We therefore discuss the output of the PCA analysis of the 6.2 μm PAH in section 5.2. We also avoid the 7.7 μm due to the blending with many emission lines such as [NeVI] (7.65 μm) and the complex continuum in this region of the mid-infrared. Therefore our analysis of the 3.3, 11.3 and 17.0 μm features are strongly dominated by the neutral PAHs.

We expand on earlier work of Donnan et al. (2024) by including the longer wavelength PAH features. These provide challenges as the 11.3 μm and 17.0 μm PAHs are broader than the 3.3 μm PAH and also have a poorer spatial resolution. However the larger field of view

compensates for this loss, where the greater number of spatial pixels results in more information available for the PCA decomposition. By probing different PAH bands, we are sensitive to different PAH molecules. The 3.3 μm PAH originates mainly from small grains while the 11.3 μm feature is dominated by larger, neutral grains (e.g. Rigopoulou et al. 2021). The 6.2 μm PAH mainly originates from ionised PAHs.

As described in section 3, velocity maps can be recovered from the principal components, where the first component contains the rest-frame emission while the higher order components and in particular the second component, contain the information about the velocity field. We show the resulting velocity maps for all the features described above in Fig. 2.

4.1.1 Ionised Gas

We use the [NeVI] (7.65 μm , 158 eV) emission line to trace highly ionised gas due to AGN photoionisation (e.g. Zhang et al. 2024a). Some of the targets, such as NGC 5506 and NGC 7172 are edge-on galaxies, where the ionisation cone extends to the north and south of the disk (e.g. Hermosa Muñoz et al. 2024) and therefore there very little of the velocity field is along the line of sight making the outflow kinematics difficult to detect. We also find MCG-05-23-016 to provide a weak detection, where the emission is point-like and associated with the nucleus.

For NGC 7582 we opt to use [NeV] (14.32 μm 77.4 eV) instead of [NeVI] as the signal to noise is higher making the kinematics of the outflow much clearer (Veenema & et al. submitted 2026).

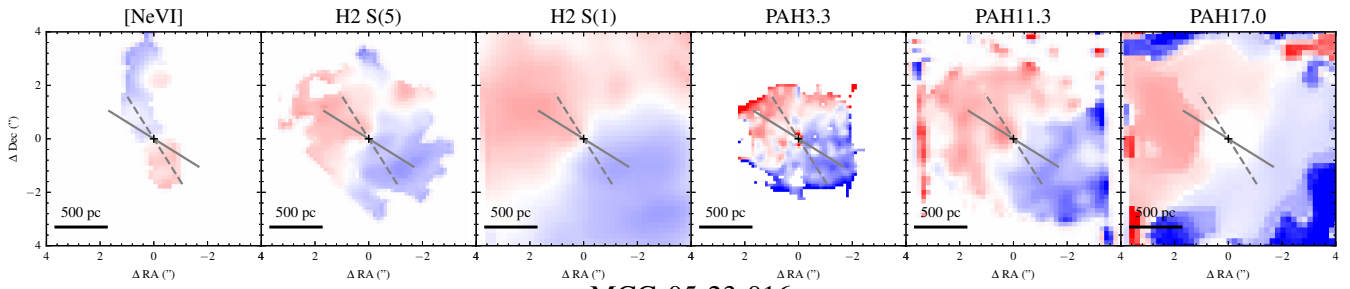
4.1.2 Molecular Gas

The hot molecular gas is traced by the H_2 S(5) line while cooler molecular gas is traced by the H_2 S(1) line. The H_2 kinematics are typically dominated by rotation in the galaxy disk, however the S(5) line appears to show contribution from the outflow in ESO 137-G034, NGC 5728 and NGC 7582. This result was presented by Davies et al. (2024) for NGC 5728 while Veenema et al. (2025) presents analysis of NGC 7582.

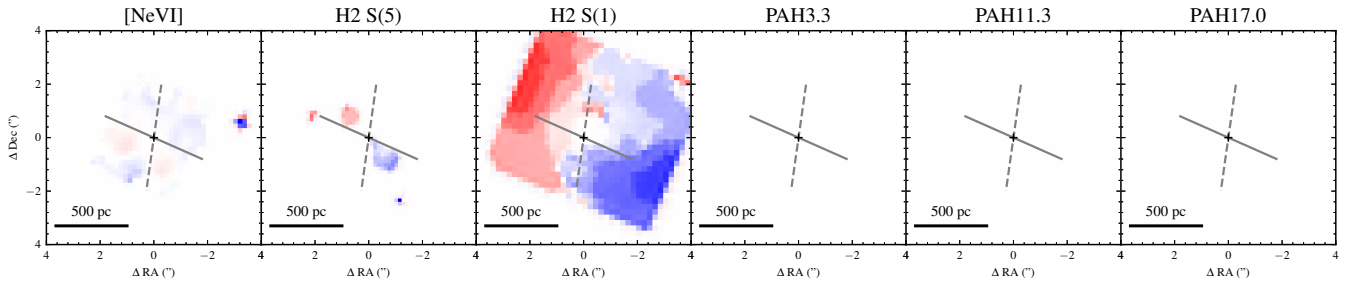
The increase in the contribution of the outflow results in the position angle of the kinematic axis changing from the S(1) to the S(5) line. For NGC 7582, the picture is less clear for the H_2 lines. This is partly due to the asymmetric FOV of the hotter H_2 lines, making it difficult to fully observe the kinematics. Moreover, the flux of the H_2 lines is strongly dominated by two star-forming regions to the south east (Veenema et al. 2025), which also show excess blueshifted velocities in the molecular gas (Veenema et al. 2025; García-Burillo et al. 2021). However we do see some excess redshifted emission towards the north east consistent with the velocity map of [NeV] which may suggest a small outflow contribution in the H_2 lines for NGC 7582. This is investigated further in section 4.2. Alternatively, García-Burillo et al. (2021) suggests that the redshifted excess may result from the projection of local inflowing gas considering they coincide with the passage of spiral arms along the minor axis.

As with the ionised gas, the edge-on nature of NGC 5506 and NGC 7172 makes it challenging to detect their outflows kinematically. The remaining objects, ESO 420-G13, MCG-05-23-16, NGC 3081, NGC 3227 and NGC 4051 do not show any detectable contribution to the outflow in the molecular gas as traced by the rotational transitions of H_2 (Esparza-Arredondo et al. 2025).

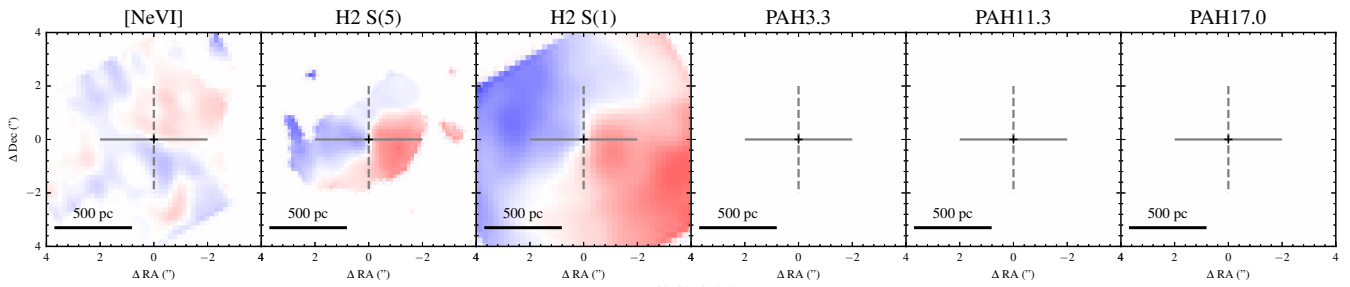
ESO 420-G13



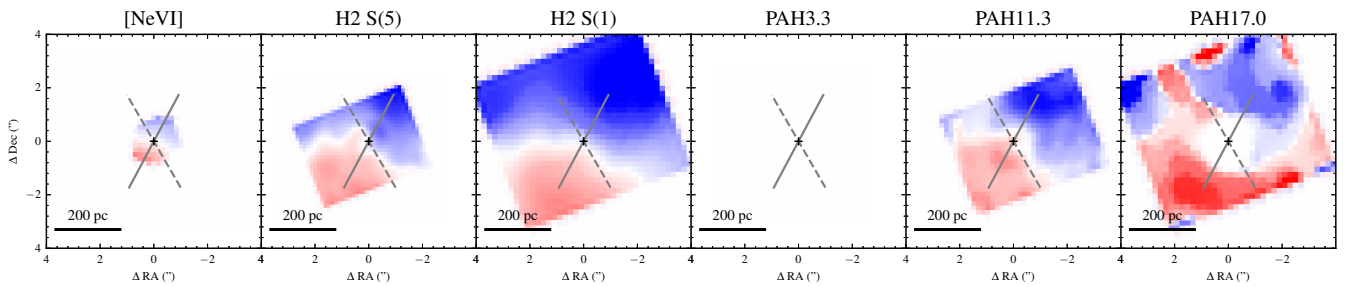
MCG-05-23-016



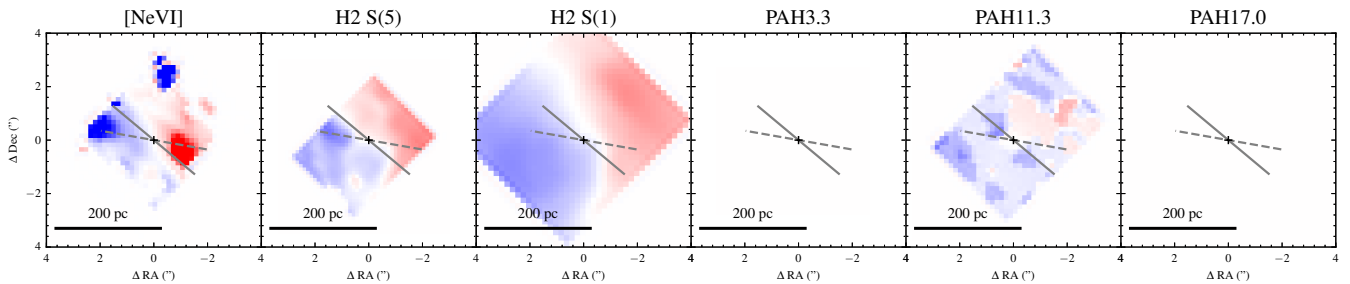
NGC 3081



NGC 3227



NGC 4051



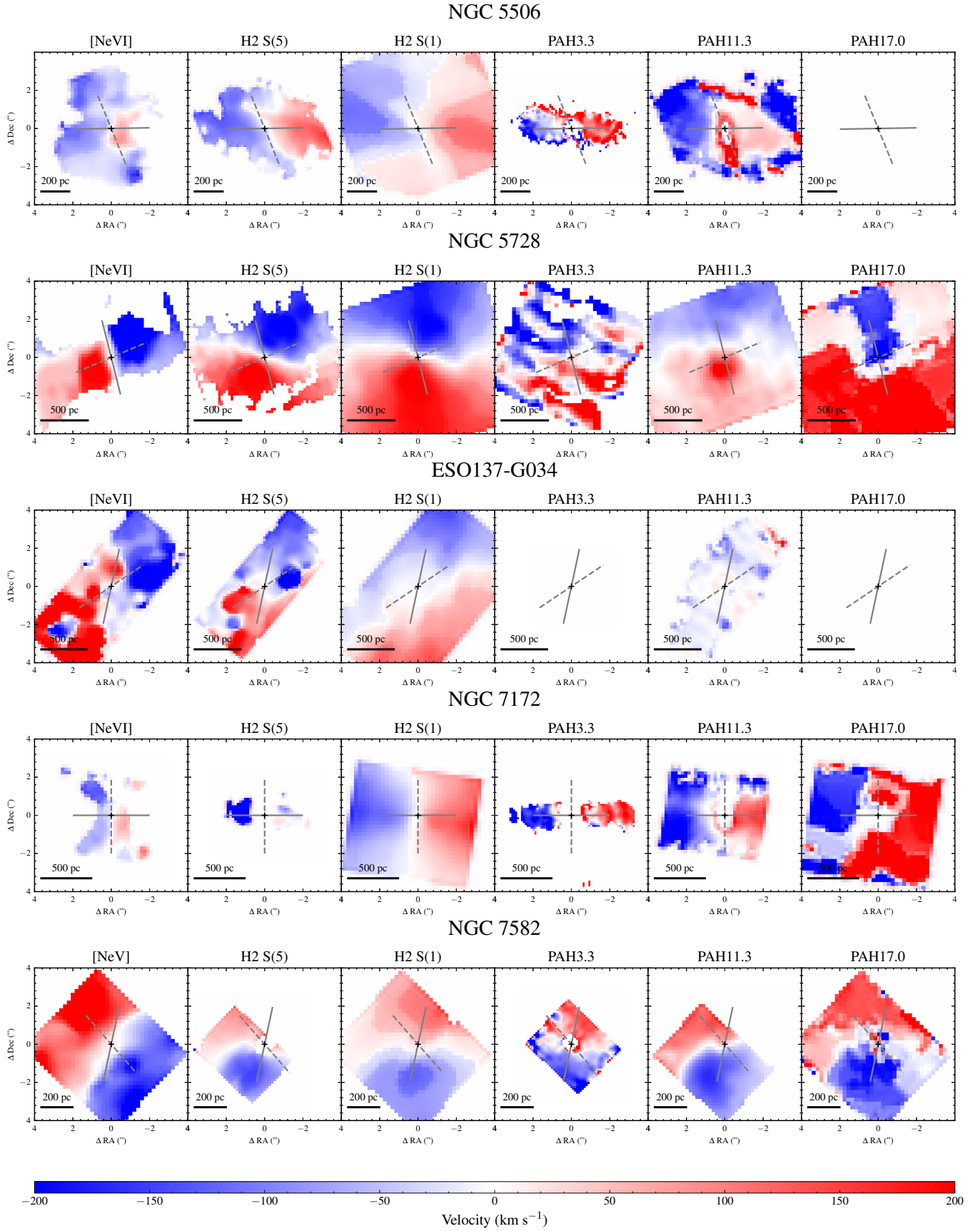


Figure 2. Velocity maps of each spectral feature for each galaxy. From left to right we show [NeVI] ($7.65 \mu\text{m}$), H₂ S(5) ($6.91 \mu\text{m}$), H₂ S(1) ($17.03 \mu\text{m}$), $3.3 \mu\text{m}$ PAH, $11.3 \mu\text{m}$ PAH and the $17 \mu\text{m}$ PAH. For each galaxy the field of view is the same for each map as well as the velocity scale. We show [NeV] ($14.32 \mu\text{m}$) for NGC 7582 as the [NeVI] ($7.65 \mu\text{m}$) has a lower signal to noise. The position angle of the major axis of the disk is shown with the solid line while the position angle of the major axis for the outflow is shown with the dashed line. Values are found in Table 1. Panels that are blank lack the signal to noise to produce velocity maps.

4.1.3 PAHs

In objects where the signal-to-noise of the $3.3\ \mu\text{m}$ PAH is high enough to be detected, the velocity is consistent with rotation in the circumnuclear disk and shows no detectable outflow contribution in any of the objects. However the $11.3\ \mu\text{m}$ and $17.0\ \mu\text{m}$ PAHs are more consistent with the rotational H_2 transitions than the ionized gas and show contribution from the outflow in two objects: NGC 5728 and NGC 7582. We see no evidence for the outflow in the PAH velocity maps of NGC 3227, NGC 4051 and ESO 420-G13. The remaining objects, MCG-05-23-016, NGC 3081, NGC 5506, ESO 137-G034 and NGC 7172 either lack the signal to noise or appear edge-on, meaning we cannot rule out the presence of PAHs in their outflows, but currently are hard to detect.

In NGC 5728, the $11.3\ \mu\text{m}$ PAH shows excess redshifted emission in the redshifted side of the outflow. In NGC 7582 the outflow is even clearer, with the $11.3\ \mu\text{m}$ PAH velocity map dominated by the outflow, consistent with the hot molecular gas as traced by the $\text{H}_2\ \text{S}(5)$ line. This is the first spatially resolved kinematic evidence of dust in the outflow of an AGN.

For NGC 5728, the $11.3\ \mu\text{m}$ PAH shows rotation consistent with circumnuclear disk but also clear redshifted emission at the base of the redshifted side of the outflow. However the blueshifted side of the outflow does not appear to be present in the $11.3\ \mu\text{m}$ velocity map. As this part of the outflow is behind and obscured by the star-forming ring (e.g. [Davies et al. 2024](#)), the velocity signature may be difficult to detect. Unlike the H_2 lines or ionised gas where the outflow is bright in the flux (moment 0) map, the PAHs are significantly brighter in the star-forming ring than in the outflow. This means the velocity (moment 1) signal of the outflow within the data is much less significant (due to the flux differences) than the disk in this region for the PAH features, while the H_2 lines and ionised lines have bright flux in the outflow, making the blueshifted velocity signal much easier to detect despite the obscuration by the star-forming ring.

The velocity map of the $17.0\ \mu\text{m}$ PAH is noisier, however it does show a clear warp in the position angle of the kinematic axis, where there is excess redshifted emission due to the outflow. We investigate the kinematic signature of the outflow in the PAH velocity maps further in section 4.2 where we isolate the outflow and disk components.

The velocity maps of the $11.3\ \mu\text{m}$ and $17.0\ \mu\text{m}$ PAHs for NGC 7582 show clear contribution from the outflow, where the redshifted emission to the north east is from the outflow whereas the redshifted emission to the north west is from the disk. In-fact, the $11.3\ \mu\text{m}$ PAH appears to be dominated by the outflow, closer matching the [NeV] velocity map rather than the $3.3\ \mu\text{m}$ PAH velocity map. The $3.3\ \mu\text{m}$ PAH only shows the kinematics of the disk, where only the redshifted emission to the north west is present. We also investigate this object further in section 4.2 by modelling the disk kinematics.

4.2 Disk Modelling

As the signal to noise of NGC 7582 and NGC 5728 is sufficiently high and show potential evidence of outflow in the kinematics of the $11.3\ \mu\text{m}$ PAH, we opt to model and subtract the disk kinematics to reveal the outflow kinematics. This was demonstrated in [Davies et al. \(2024\)](#), where the velocity maps of H_2 contain contribution from both the circumnuclear disk and the outflow. To recover the outflow component, one can model the velocity field of the disk and subtract from the observed velocity map of a given feature.

We follow [Veenema & et al. submitted \(2026\)](#) and fit a disk model

at a fixed inclination and position angle constrained from previous observations. The free parameters of the model are the parameters governing the intrinsic radial velocity curve, $V(R)$, which has the form of a tanh function allowing the rotation curve to rise steeply at low radii and then flatten at larger radii,

$$V(R) = V_{\text{max}} \tanh\left(\frac{R}{R_{\text{turn}}}\right), \quad (4)$$

where the V_{max} and R_{turn} are free parameters. The observed velocity, $V_{\text{obs}}(x, y)$, of each spaxel (x, y) is therefore

$$V_{\text{obs}}(x, y) = V_{\text{sys}} + V(R) \sin i \cos \theta, \quad (5)$$

where $V(R)$ is the velocity of each ring at radius R and V_{sys} is the systemic velocity. The radius, R , is the intrinsic, deprojected radius which relates to the coordinates of each spaxel (x, y) via

$$\begin{aligned} x' &= x \cos \phi + y \sin \phi, \\ y' &= -x \sin \phi + y \cos \phi, \\ R &= \sqrt{x'^2 + \left(\frac{y'}{\cos i}\right)^2}, \\ \cos \theta &= \frac{x'}{R}, \end{aligned}$$

where ϕ is the position angle of the disk on the sky.

Typically one can fit a velocity model, such as the tilted ring model, to a 3D data cube using codes such as 3D-Barolo ([Di Teodoro & Fraternali 2015](#)), modelling both the moment 0 and moment 1 maps of a given feature. However we fit to the 2D velocity maps (moment 1) of a given feature instead as the PAH features, unlike emission lines, have an intrinsic broad profile. We fit each of the velocity maps for every emission feature in NGC 5728 and NGC 7582, using MCMC sampling from NUMPYRO ([Phan et al. 2019](#)).

For NGC 5728, the geometry of the disk is well constrained from both the CO (2-1) velocity field and the stellar kinematics ([Shimizu et al. 2019](#)). We found that directly using the disk models presented in [Shimizu et al. \(2019\)](#), over-predicted the rotation velocity for the $11.3\ \mu\text{m}$ PAH feature. We therefore fix the position angle/inclination contained by the stellar/CO kinematics of $\text{PA} = 14^\circ$, $i = 43^\circ$ and fit for the rotational velocity. We present the results of the disk modelling for NGC 5728 in Fig. 3.

For NGC 7582 we use the position angle constrained from the low ionisation potential lines in the MIRI data from [Veenema & et al. submitted \(2026\)](#) of $\text{PA} = 221^\circ$. We use an inclination of $i = 58^\circ$ ([Morris et al. 1985](#); [Wold et al. 2006](#)) consistent with [Veenema & et al. submitted \(2026\)](#) and the stellar kinematics presented in [Juneau et al. \(2022\)](#). We fix the inclination and position angle of the disk in our fitting using the above values.

This results in the disk models shown in Fig. 4. Subtracting the disk model from the observed velocity map results in the right hand column of Fig. 4. We additionally shift the systemic velocity of the $\text{H}_2\ \text{S}(5)$, $\text{H}_2\ \text{S}(1)$ and the $11.3\ \mu\text{m}$ PAH, by adding the systemic velocity as a free parameter to the disk fitting, as the maps appear to be dominated by redshifted emission. This is likely a result of the field of view being off-centre, where the emission is therefore dominated by the blueshifted side of the disk. This leads to the first principal component appearing too blue and therefore the wavelengths shifts for each spaxel are redder resulting in a map offset to positive velocities.

We find that the $3.3\ \mu\text{m}$ PAH is fit well by the disk model, with the residuals not showing any clear outflow signature. The opposite picture is true however for the $11.3\ \mu\text{m}$ PAH, where the position angle of the velocity map is much more consistent with [NeV] than the disk kinematics ([Juneau et al. 2022](#)), even without modelling the

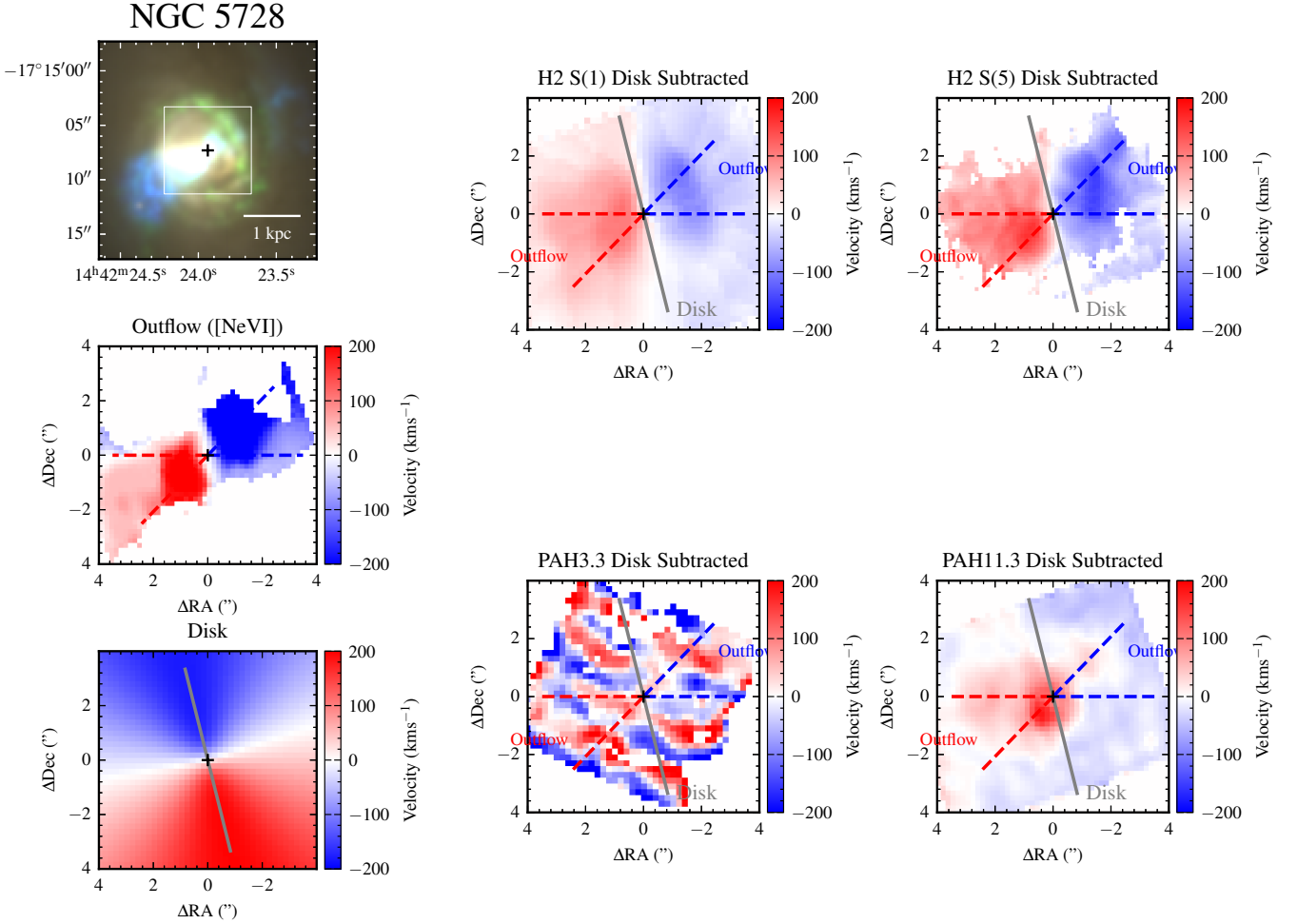


Figure 3. Disk modelling and subtraction for NGC 5728. The top left panel shows a three color image constructed from custom filters of MUSE cubes. Blue is a filter centred on [O III] (5028–5095 Å), green is H α (6578–6664 Å) and an *i* band filter (6430–8630 Å) is shown in red. The white square shows the FOV of the other panels. The middle left panel shows the velocity map of [NeVI] tracing the outflow. The bottom left panel shows the disk model with fixed inclination and position angle constrained from CO and stellar kinematics (Shimizu et al. 2019). The right panels show the disk subtracted velocity maps for molecular gas (warm S(1) and hot S(5)) as well as the 3.3 μ m PAH (small & neutral) and the 11.3 μ m PAH (large & neutral). The major axis of the disk is shown with the solid grey line while the outflow cone is shown with the dashed lines in red and blue for the redshift and blueshift sides of the cone respectively.

disk component. The 17 μ m PAH also shows excess redshifted and blueshifted velocities consistent with [NeV] but has a stronger disk component than the 11.3 μ m PAH.

As mentioned previously, the outflow is not as clear in the H $_2$ lines for NGC 7582. The residuals of the H $_2$ S(5) line do show residual redshifted gas consistent with the outflow however there is also an excess of blueshifted gas to the south east, coincident with H $_2$ bright star-forming regions (Veenema et al. 2025). From CO lines, García-Burillo et al. (2021) points out that the excess redshifted and blueshifted velocities in the H $_2$ lines could be the projection of local inflows rather than outflows, considering the coincidence with spiral arms along the minor axis of the disk. However they also do note that there are coplanar outflow motions in the cold H $_2$ as well albeit on small scales.

We further demonstrate the effect of the contribution of the outflow to the observed velocity maps in Fig. 5, where we take the pure disk model and add the outflow with progressively higher contributions. We find that the 15% outflow contribution provides a good match to the H $_2$ S(1) line while the 25% outflow map matches the hotter H $_2$ S(5) line. for both NGC 5728 and NGC 7582. The 11.3 μ m PAH

matches a higher outflow contribution at up to 50 % for both targets, although for NGC 5728 is missing the blueshifted side as previously discussed. The 17 μ m PAH shows a similar velocity map to the H $_2$ S(5) line, with an outflow contribution of $\sim 25\%$, although the map is very noisy for NGC 5728.

5 DISCUSSION

5.1 Dust in AGN Outflows

From the analysis in section 4.2, the outflow signature is clear in the velocity map of the 11.3 μ m PAH in both NGC 7582 and NGC 5728. The other PAH features show much weaker evidence of the outflow however the 17.0 μ m PAH also shows evidence of the outflow after subtracting the disk model. We discuss the implications on the properties of the PAH molecules in section 5.2. We do not find any evidence of the outflow in the PAH velocity maps for ESO 420-G13 however.

The picture is similar for the molecular gas as seen by the rotational transitions of H $_2$. Both NGC 7582 and NGC 5728 show

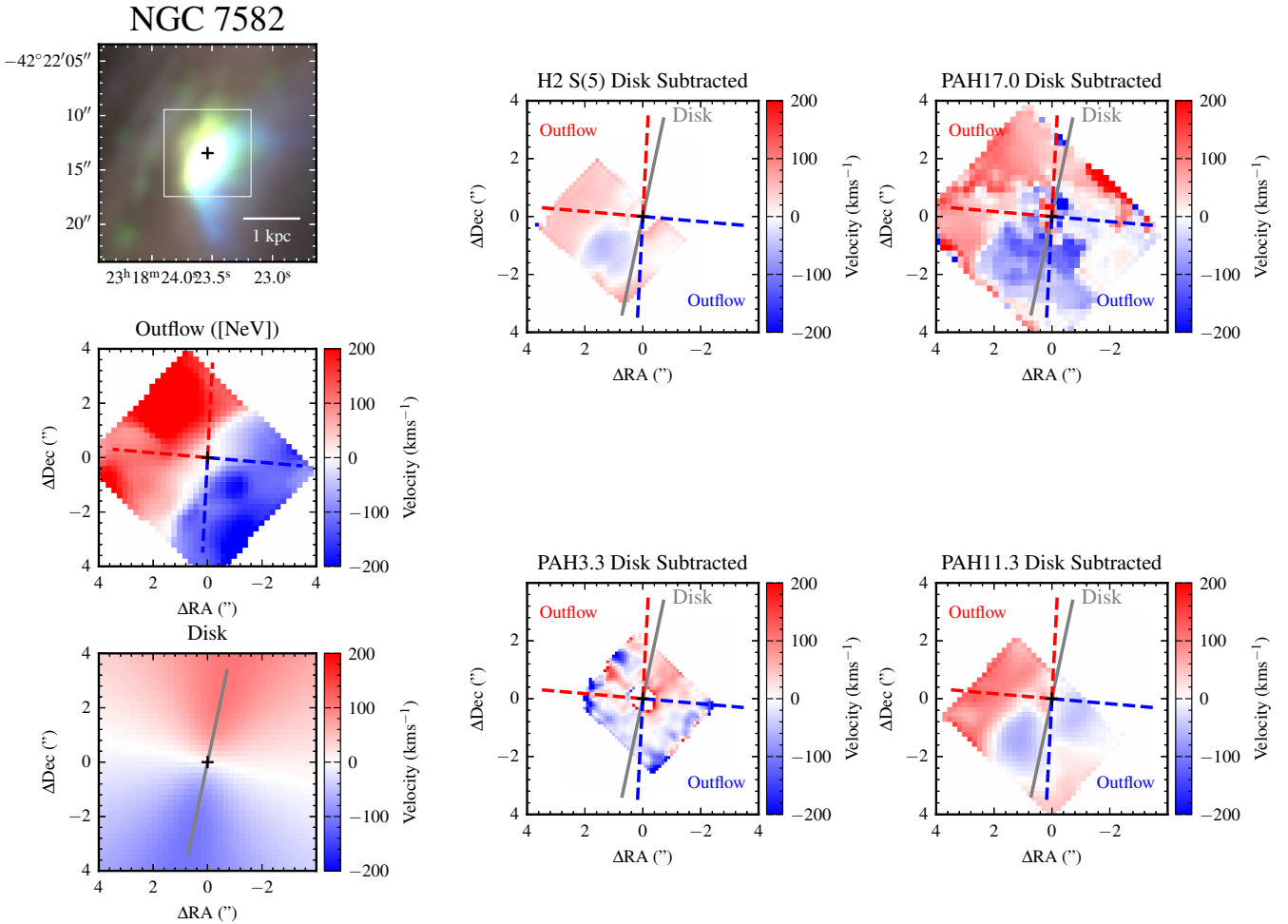


Figure 4. Disk modelling and subtraction for NGC 7582. The top left panel shows a three color image constructed from custom filters of MUSE cubes. Blue is a filter centred on [O III] (5028–5095 Å), green is H α (6578–6664 Å) and an i band filter (6430–8630 Å) is shown in red. The white square shows the FOV of the other panels. The middle left panel shows the velocity map of [NeV] tracing the outflow. The bottom left panel shows the disk model with fixed inclination and position angle. The right panels show the disk subtracted velocity maps for molecular gas (S(5)) as well as the 3.3 μ m PAH (small & neutral), the 11.3 μ m PAH (large & neutral) and the 17 μ m PAH (large & neutral). The major axis of the disk is shown with the solid grey line while the outflow cone is shown with the dashed lines in red and blue for the redshift and blueshift sides of the cone respectively.

a combination of disk and outflow in the molecular gas, with the higher-J rotational transitions containing a greater contribution from the outflow. The only other target that shows clear evidence for the presence of the outflow in the H $_2$ rotational lines in ESO 137-G034. Unfortunately the signal to noise of the PAH features is low in this target and so we cannot verify if there are PAHs in the outflow. The remaining targets show no clear evidence of either H $_2$ or PAHs in the outflow which does not rule out their presence. The lack of detection may be due to the galaxy being viewed edge-on which is the case for NGC 5506 and NGC 7172 or the outflow kinematics are not distinct from rotation. This is the case for NGC 3227. However ESO 420-G13, NGC 3081 and NGC 4051 show no evidence for the outflow in the kinematics of the rotational H $_2$ lines or the PAHs (where the signal to noise is sufficient).

The correlation between PAH emission and molecular gas content (e.g. Regan et al. 2006; Cortzen et al. 2019; Shivaei & Boogaard 2024) is well documented, typically attributed to star-forming regions however this is also the case in outflows for both star-formation driven outflows such as in M82, (Beirão et al. 2015; Lopez et al. 2025;

Villanueva et al. 2025) but also AGN outflows (e.g. García-Bernete et al. 2024).

5.1.1 Acceleration of dust grains

To investigate the acceleration of the PAHs in the outflow we extract the velocity profile of the 11.3 μ m PAH feature after subtracting the disk kinematics. We plot this in Fig. 6 alongside the molecular gas via the H $_2$ S(5) and S(1) lines. We show the distance as both observe angular distance in arcseconds as well as the deprojected distance assuming an outflow inclination of 49° (Shimizu et al. 2019).

The profiles clearly show an initial acceleration before a deceleration out to ~ 1 kpc. For the molecular gas, the acceleration takes place up to ~ 0.3 kpc before the deceleration, with the S(5) line reaching tracing higher velocity gas. The PAH feature however shows a quicker acceleration and an earlier deceleration at ~ 0.1 kpc. This is expected as PAHs have a higher surface area to mass ratio than molecular gas, making them easier to radiatively accelerate close to the AGN (e.g. Fabian et al. 2008), but also easier to decelerate as material is swept up from the ISM into the outflow. This scenario

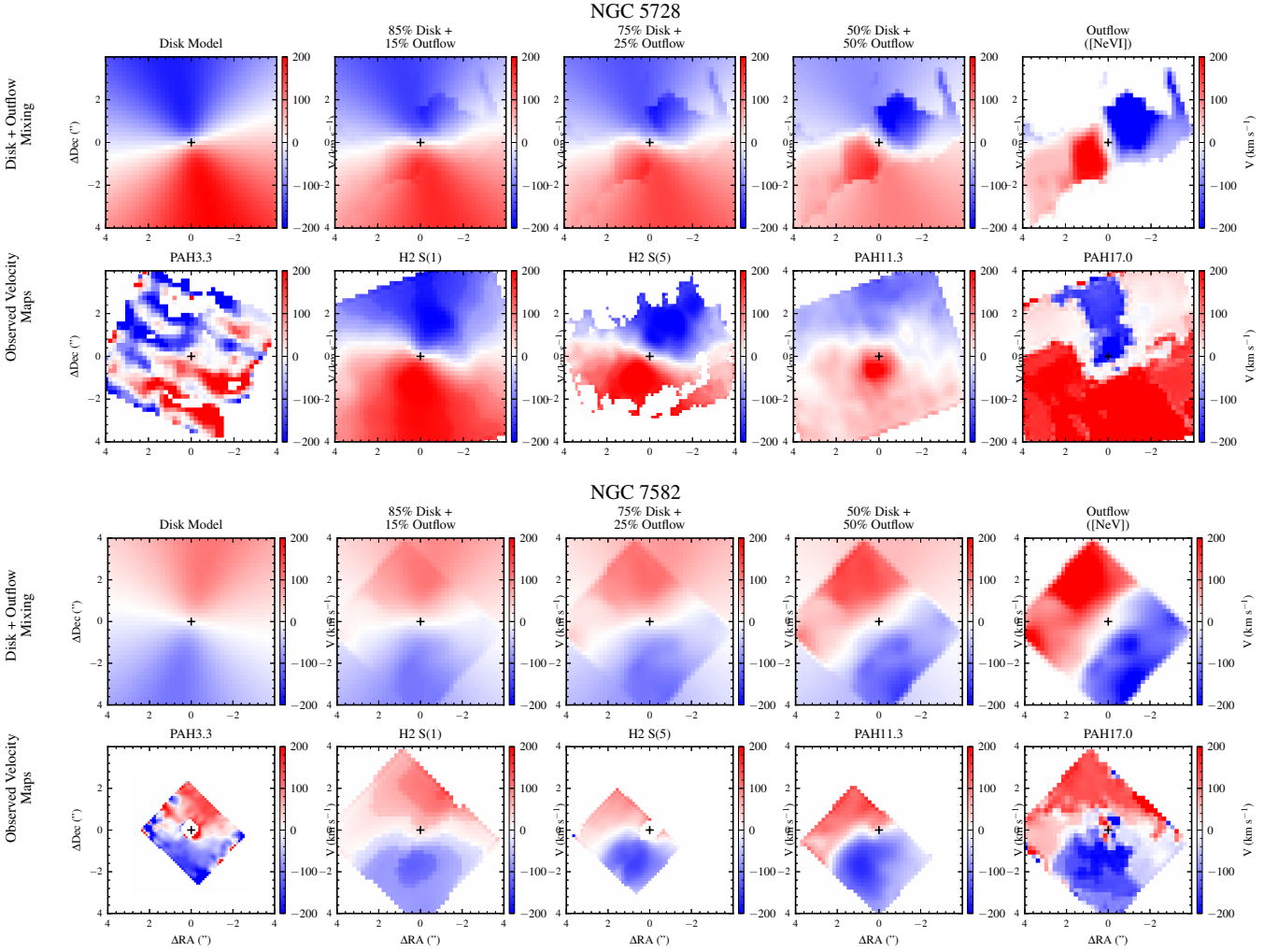


Figure 5. Demonstration of the effect of various contributions of the outflow and disk on the resultant velocity map. The top two panels are for NGC 5728 while the bottom two are for NGC 7582. For each object the top row shows the progression from left to right of the velocity map from pure disk to pure outflow. The lower panels show observed velocity maps for various features where the 3.3 PAH on the left shows pure disk while the other features show some mixture of outflow and disk.

assumes radiative acceleration but considering the relatively larger scales of this outflow ($\gtrsim 100$ pc), acceleration due to a jet or AGN winds is also plausible. NGC 5728 has a radio detected jet on scales of > 200 pc (Schommer et al. 1988; Durré & Mould 2018) however evidence for a jet in NGC 7582 is more tentative (Forbes & Norris 1998; Ricci et al. 2018).

The drop in velocity of the PAHs with distance could also be due to destruction due to shocks where as PAHs are accelerated to high speed, they become susceptible to shocks at velocities of $\gtrsim 100$ km s^{-1} (e.g. Micelotta et al. 2010; Donnan et al. 2023), causing only slow moving PAHs to remain at higher distances from the AGN.

5.1.2 Dust Origin

With this kinematic evidence for PAHs it is clear that dust forms part of the outflow from AGN however a key question still remains. Does the dust originate from the torus and forms part of the polar dust structure (e.g. Hönl 2019) or does the dust simply reside in the ISM and is entrained in the ISM of the host galaxy (e.g. Alonso-Herrero et al. 2019; Shimizu et al. 2019; García-Bernete et al. 2021)?

One argument for the latter is from PAH band ratios, where AGN

outflows show more neutral PAHs (e.g. García-Bernete et al. 2024) however this only appears to happen when there is strong coupling/interaction between the outflow and the circumnuclear star-forming disk. This is the case for both NGC 5728 and NGC 7582 (e.g. García-Bernete et al. 2024; García-Bernete & et al. in prep 2026; Veenema & et al. submitted 2026). Considering that the outflows we have detected are on larger scales (~ 1 kpc) than the torus (~ 10 s pc García-Burillo et al. 2019, 2021; Combes et al. 2019; Alonso-Herrero et al. 2021), suggests that these dusty outflows arise from the interaction of the AGN with its circumnuclear environment.

We can further address this question by inspecting the position of the galaxies on the column density, N_{H} , vs Eddington ratio, λ_{Edd} diagram. This was first introduced by Fabian et al. (2008), where the effective Eddington limit for dust is lower than the gas, resulting in a region of the N_{H} vs λ_{Edd} space where the AGN clear all of their dust (e.g. Ricci et al. 2017). For the GATOS sample, this kind of diagram was first shown in Alonso-Herrero et al. (2021). We determine the hydrogen column density from CO observations from García-Burillo et al. (2024), assuming a Milky Way α_{CO} and CO line ratios consistent with the highest spatial resolution data of NGC 1068 (García-Burillo et al. 2014; Viti et al. 2014). We plot the hydrogen column density

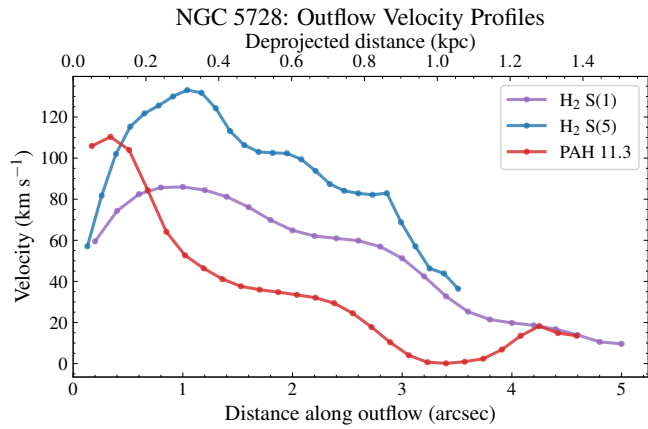


Figure 6. Velocity profiles of the molecular gas via the H₂ S(1) and H₂ S(5) lines compared to the 11.3 μm PAH feature. These were extracted after subtracting the disk kinematics and only for the red side of the outflow.

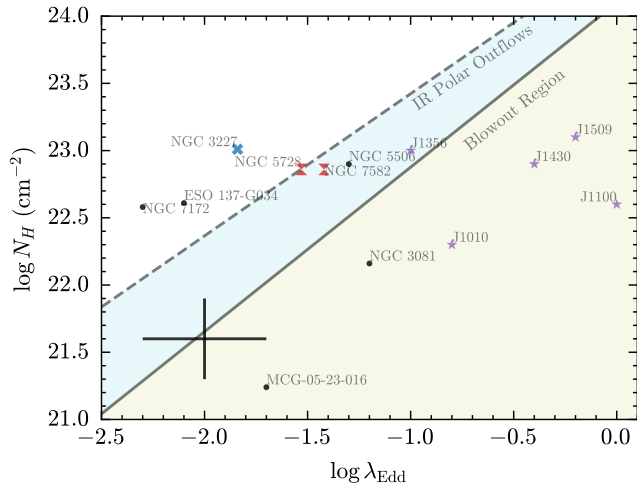


Figure 7. Diagram of the column density, N_H , vs the Eddington ratio, λ_{Edd} . The column densities are inferred from CO in [García-Burillo et al. \(2024\)](#). The sources that show PAHs in the outflow are marked with a red hourglass marker while the object where we rule out PAHs in the outflow is shown with a blue cross. Objects where we do not see any evidence for PAHs in the outflows but cannot rule out their presence are shown with the black circles. We also plot the quasars from [Ramos Almeida et al. \(2025b,a\)](#) as purple stars for reference. We show the limit from [Fabian et al. \(2008\)](#) (solid line) beyond which the Eddington ratio exceeds the effective Eddington ratio for dust creating the “Blowout Region”. We also show the limit from [Venanzi et al. \(2020\)](#) (dashed line) where gravity balances the radiation pressure, creating a parameter space where we would expect to see polar outflows. The cross in the bottom left corner shows typical uncertainties in both axes.

against the Eddington ratio in Fig. 7. It is worth noting that there is a lot of uncertainty in measuring the column density as different CO lines and/or X-ray data will give different results. We therefore show a wide error range in Fig. 7. Moreover, the line of sight can affect the measured value of N_H . We show the theoretical regions for polar dust outflows from [Venanzi et al. \(2020\)](#) and the blowout region from [Fabian et al. \(2008\)](#).

We find that the two sources that show PAHs in the outflow, NGC 5728 and NGC 7582, are consistent with the polar outflow region of the plot, although the large errors should be noted. The other sources are spread throughout the parameter space with NGC 3227, which

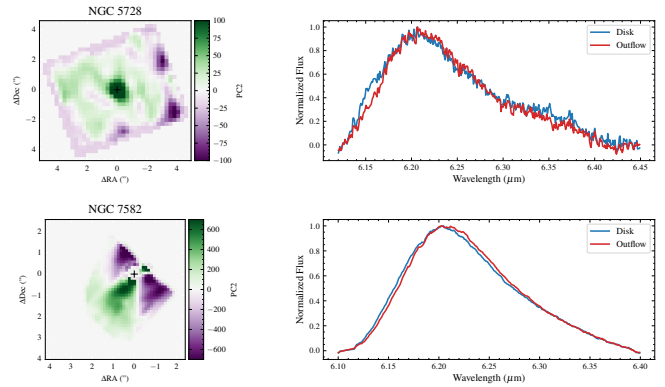


Figure 8. The second principal components of the 6.2 μm PAH features for NGC 5728 and NGC 7582. The left panels show the tomograms while the right panels show the PAH profiles for regions where the tomogram is either positive or negative, corresponding to different intrinsic profiles in the galaxy disk or outflow. We use a different colourscale to differential from velocity.

we rule out showing PAHs in the outflow, appearing outwith the polar outflow region. This may suggest that the outflows originated from the torus however the presence of coupling in the two sources that show PAHs in the outflow also suggests that the interaction of the outflow with the circumnuclear ISM may also be necessary to entrain material into the outflow.

A more observationally driven parameter space presented by [García-Burillo et al. \(2024\)](#) is the molecular gas concentration vs X-ray luminosity, where the gas concentration is the ratio of the molecular surface density at 50 pc to 200 pc. In this plot, two regions are observed, the “AGN build-up” where at low X-ray luminosity the gas concentration increases and the “AGN feedback” branch, where at high X-ray luminosity the gas concentration decreases. This diagram probes larger scales than the N_H , vs λ_{Edd} , up to 200 pc, where all the sources in our sample are in the “Feedback Branch”. This makes it unsurprising that we find

5.2 PAH Properties

The properties of PAHs are known to be altered in the vicinity of AGN outflows ([García-Bernete et al. 2022a,b, 2024](#); [Rigopoulou et al. 2024](#); [Zhang et al. 2024b](#)), in particular appearing more neutral, signified by a relatively weaker 6.2 μm PAH emission. In this work, we found the 6.2 μm feature challenging to obtain any kinematics as the signal to noise is relatively low in the outflow region, potentially due to preferential destruction of ionised grains (e.g. [García-Bernete et al. 2024](#)), making extracting kinematics difficult. Secondly, the PCA technique is sensitive to differences in the intrinsic PAH profile, and cannot necessarily differentiate between kinematics affecting the observed profile or a different intrinsic profile. In the case of the 6.2 μm PAH, considering this feature traces PAHs heavily altered by the outflow, it makes sense that the intrinsic profile may be different in the outflow region. We show the different intrinsic profiles, albeit only with subtle differences, as detected in the second principal component for NGC 5728 and NGC 7582 in Fig. 8.

Interestingly, the 3.3 μm PAH purely traces rotation in the disk and shows no contribution from the outflow compared to the 11.3 μm PAH and 17 μm PAH. This suggests that small PAH molecules are also destroyed in the outflows of AGN. Small PAHs are thought to be easier to destroy than large PAHs (e.g. [Lebouteiller et al. 2007](#); [O’Dowd et al. 2009](#); [Micelotta et al. 2010](#); [Zhen et al. 2015](#); [Lange](#)

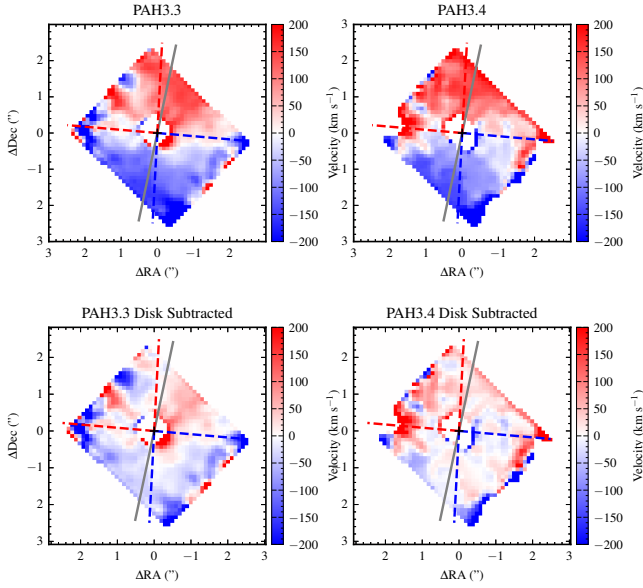


Figure 9. Top: The velocity maps of the $3.3 \mu\text{m}$ PAH feature and the $3.4 \mu\text{m}$ aliphatic feature for NGC 7582. Bottom: Disk subtracted velocity maps of the $3.3 \mu\text{m}$ PAH feature and the $3.4 \mu\text{m}$ aliphatic feature. The major axis of the disk is shown with the solid grey line while the outflow cone is shown with the dashed lines in red and blue for the redshift and blueshift sides of the cone respectively.

et al. 2025), suggesting that the radiation field of the AGN preferentially destroys small grains.

Large and neutral PAH molecules are consistent with PAH band ratios measured for Seyfert galaxies (García-Bernete et al. 2022a,b, 2024; Donnelly et al. 2024), where the ionised and small PAH molecules are thought to be destroyed by the radiation field of the AGN. The mechanism by which this takes place however is not fully understood but it may be related to ionised PAHs having weaker carbon skeletons due to higher Coulomb forces when electrons are lost or gained through ionisation (Leach 1986; Voit 1992), making them more susceptible to photo-destruction.

The lack of kinematics of small and ionised PAHs in the outflow provides new, corroborating evidence in addition to the band ratios, that PAHs are altered by AGN outflows becoming more neutral and larger.

5.3 Aliphatics in the Outflow?

The $3.4 \mu\text{m}$ feature results from aliphatic hydrocarbons, where instead of a closed carbon chain (aromatic), open carbon chains, either as side groups or as independent molecules, produce the feature at $3.4 \mu\text{m}$ (Wexler 1967; Duley & Williams 1981; Pauzat et al. 1999).

Given that the $3.4 \mu\text{m}$ feature is relatively weak compared to the $3.3 \mu\text{m}$ PAH feature, the signal to noise of most targets in this work is not sufficient to produce a velocity map. However for NGC 7582 we are able to produce a velocity map which is shown in Fig. 9 in comparison with the $3.3 \mu\text{m}$ PAH. We also detect the double peak in the $3.4 \mu\text{m}$ feature at $3.395 \mu\text{m}$ and $3.405 \mu\text{m}$. The strong presence of the latter feature indicates that the PAHs are shielded by molecular gas (Thatte et al. 2026).

We find no convincing evidence for the presence of the outflow in the residual velocity map of the $3.4 \mu\text{m}$ feature in Fig. 9 with the velocity well reproduced by the disk model. The $3.4 \mu\text{m}$ feature is thought to be dominated by aliphatic side groups on aromatic

molecules (Joblin et al. 1996; Pendleton & Allamandola 2002; Yang & Li 2023) and so it is not necessarily a tracer of the total aliphatic content. Therefore the lack of $3.4 \mu\text{m}$ in the outflow could be explained as the stripping of aliphatic side groups from large PAHs in the hard radiation field of the outflow (Joblin et al. 1996; Jones et al. 2013; Yang et al. 2016).

6 CONCLUSIONS

In this work we presented the kinematics of PAH features using PCA tomography for 10 nearby Seyfert galaxies as part of the GATOS sample. We present the first kinematic detection of outflowing dust from AGN. Our main findings are

- We find that the velocity field of the $3.3 \mu\text{m}$ PAH is purely due to rotation in the circumnuclear disk of the host galaxy for all our targets where $3.3 \mu\text{m}$ PAH is detected.
- We find that the $11.3 \mu\text{m}$ PAH and $17.0 \mu\text{m}$ PAH show contribution from the outflow in 2 out of the 10 targets, namely NGC 5728 and NGC 7582. After subtracting a disk model, the residuals show clear evidence of the outflow.
- The $6.2 \mu\text{m}$ PAH fails to produce a velocity map from the PCA tomography technique, with instead the PCA showing an alternative intrinsic profile in the outflow regions suggesting the ionised PAHs are altered in AGN outflows. This fact as well as the lack of $3.3 \mu\text{m}$ PAH in the outflow is consistent with band ratios that suggest AGN outflows contain more neutral and larger PAHs than star-forming regions.
- We find that the objects that show PAHs in the outflow also show outflow contributions in the molecular gas as traced by the H_2 rotational transitions. This suggests that the PAHs are correlated with the molecular gas in AGN outflows.
- We find a lack of evidence for the $3.4 \mu\text{m}$ aliphatic feature in AGN outflows, consistent with the idea of stripping of aliphatic side groups in the hard radiation fields of AGN outflows.

We suggest that the presence of PAHs in AGN outflows is the result of the interaction and coupling to the circumnuclear environment where material is entrained into the outflow. This kind of work presents the first kinematic analysis of a new phase of AGN outflows. Expanding the sample to cover a wider parameter space will enable us to understand how the dusty phase of AGN outflows which is potentially linked to how AGN evolve and clear their obscuring dust.

ACKNOWLEDGEMENTS

FRD acknowledges support from STFC through studentship ST/W507726/1. IGB is supported by the Programa Atracción de Talento Investigador “César Nombela” via grant 2023-T1/TEC-29030 funded by the Community of Madrid, and acknowledges support from the research project PID2024-159902NA-I00 funded by the Spanish Ministry of Science and Innovation/State Agency of Research (MCIN/AEI/10.13039/501100011033) and FSE+. DR acknowledges support from STFC through grant ST/S000488/1 and ST/W000903/1. RAR acknowledges the support from the Conselho Nacional de Desenvolvimento Científico e Tecnológico (CNPq; Projects 303450/2022-3, and 403398/2023-1), the Coordenação de Aperfeiçoamento de Pessoal de Nível Superior (CAPES; Project 88887.894973/2023-00), and Fundação de Amparo à Pesquisa do Estado do Rio Grande do Sul (FAPERGS; Project 25/2551-0002765-9). JAFO acknowledges financial support by the Spanish Ministry of

Science and Innovation (MCIN/AEI/10.13039/501100011033), by “ERDF A way of making Europe” and by “European Union NextGenerationEU/PRTR” through the grants PID2021-124918NB-C44 and CNS2023-145339; MCIN and the European Union – NextGenerationEU through the Recovery and Resilience Facility project ICTS-MRR-2021-03-CEFCA. MS acknowledges support by the Ministry of Science, Technological Development and Innovation of the Republic of Serbia (MSTDIRS) through contract no. 451-03-136/2025-03/200002 with the Astronomical Observatory (Belgrade). CRA and AA thank the Agencia Estatal de Investigación of the Ministerio de Ciencia, Innovación y Universidades (MCIU/AEI) under the grant “Tracking active galactic nuclei feedback from parsec to kiloparsec scales”, with reference PID2022-141105NB-I00 and the European Regional Development Fund (ERDF). AA also acknowledges support from the European Union (WIDERA ExGal-Twin, GA 101158446). CR acknowledges support from SNSF Consolidator grant F01-13252, Fondecyt Regular grant 1230345, ANID BASAL project FB210003 and the China-Chile joint research fund. SGB acknowledges support from the Spanish grant PID2022-138560NB-I00, funded by MCIN/AEI/10.13039/501100011033/FEDER, EU. MPS acknowledges support from grants RYC2021-033094-I, CNS2023-145506, and PID2023-146667NB-I00 funded by MCIN/AEI/10.13039/501100011033 and the European Union NextGenerationEU/PRTR. Acknowledgments: AJB acknowledges funding from the “FirstGalaxies” Advanced Grant from the European Research Council (ERC) under the European Union’s Horizon 2020 research and innovation program (Grant agreement No. 789056). EB acknowledges support from the Spanish grants PID2022-138621NB-I00 and PID2021-123417OB-I00, funded by MCIN/AEI/10.13039/501100011033/FEDER, EU. AAH and LHM acknowledge support from grant PID2021-124665NB-I00 funded by MCIN/AEI/10.13039/501100011033 and by ERDF A way of making Europe. O.G.-M. acknowledges the support received by the UNAM DGAPA-PAPIIT project IN109123 and SEHCITI Ciencia de Frontera project CF-2023-G100. SFH acknowledges support through UK Research and Innovation (UKRI) under the UK government’s Horizon Europe Funding Guarantee (EP/Z533920/1, selected in the 2023 ERC Advanced Grant round) and an STFC Small Award (ST/Y001656/1)

DATA AVAILABILITY

This work is based [in part] on observations made with the NASA/ESA/CSA James Webb Space Telescope. The data were obtained from the Mikulski Archive for Space Telescopes at the Space Telescope Science Institute, which is operated by the Association of Universities for Research in Astronomy, Inc., under NASA contract NAS 5-03127 for JWST. These observations are associated with programs GO 5017, GO 1875, GO 1670, GO 3335. The data are downloadable from the [MAST archive](#).

REFERENCES

- Alonso-Herrero A., et al., 2014, *MNRAS*, **443**, 2766
 Alonso-Herrero A., et al., 2019, *A&A*, **628**, A65
 Alonso-Herrero A., et al., 2021, *A&A*, **652**, A99
 Alonso-Herrero A., et al., 2023, *A&A*, **675**, A88
 Antonucci R., 1993, *ARA&A*, **31**, 473
 Antonucci R. R. J., Miller J. S., 1985, *ApJ*, **297**, 621
 Asmus D., 2019, *MNRAS*, **489**, 2177
 Asmus D., Hönig S. F., Gandhi P., Smette A., Duschl W. J., 2014, *MNRAS*, **439**, 1648
 Asmus D., Hönig S. F., Gandhi P., 2016, *ApJ*, **822**, 109
 Beirão P., et al., 2015, *Monthly Notices of the Royal Astronomical Society*, **451**, 2640
 Bentz M. C., Markham M., Rosborough S., Onken C. A., Street R., Valluri M., Treu T., 2023, *ApJ*, **959**, 25
 Bock J. J., et al., 2000, *AJ*, **120**, 2904
 Braatz J. A., Wilson A. S., Gezari D. Y., Varosi F., Beichman C. A., 1993, *ApJ*, **409**, L5
 Caglar T., et al., 2020, *A&A*, **634**, A114
 Campbell S., et al., 2025, *MNRAS*, **544**, 648
 Candian A., Sarre P. J., 2015, *MNRAS*, **448**, 2960
 Combes F., 2017, *Front. astron. space sci*, **4**
 Combes F., et al., 2019, *A&A*, **623**, A79
 Cortzen I., et al., 2019, *MNRAS*, **482**, 1618
 Davies R. I., et al., 2015, *ApJ*, **806**, 127
 Davies R., et al., 2020, *MNRAS*, **498**, 4150
 Davies R., et al., 2024, *A&A*, **689**, A263
 Denney K. D., et al., 2009, *ApJ*, **702**, 1353
 Di Teodoro E. M., Fraternali F., 2015, *MNRAS*, **451**, 3021
 Donnan F. R., García-Bernete I., Rigopoulou D., Pereira-Santaella M., Alonso-Herrero A., Roche P. F., Hernán-Caballero A., Spoon H. W. W., 2023, *MNRAS*, **519**, 3691
 Donnan F. R., Rigopoulou D., García-Bernete I., 2024, *MNRAS*, **532**, L75
 Donnelly G. P., Smith J. D. T., Draine B. T., Togi A., Lai T. S.-Y., Armus L., Dale D. A., Charmandaris V., 2024, *ApJ*, **965**, 75
 Duley W. W., Williams D. A., 1981, *MNRAS*, **196**, 269
 Durré M., Mould J., 2018, *ApJ*, **867**, 149
 Esparza-Arredondo D., et al., 2025, *A&A*, **693**, A174
 Fabian A. C., 2012, *ARA&A*, **50**, 455
 Fabian A. C., Vasudevan R. V., Gandhi P., 2008, *MNRAS*, **385**, L43
 Fernández-Ontiveros J. A., et al., 2020, *A&A*, **633**, A127
 Fischer T. C., Crenshaw D. M., Kraemer S. B., Schmitt H. R., 2013, *ApJS*, **209**, 1
 Forbes D. A., Norris R. P., 1998, *MNRAS*, **300**, 757
 Gámez Rosas V., et al., 2022, *Nature*, **602**, 403
 García-Bernete I., et al. in prep 2026
 García-Bernete I., et al., 2021, *A&A*, **645**, A21
 García-Bernete I., Rigopoulou D., Alonso-Herrero A., Pereira-Santaella M., Roche P. F., Kerkeni B., 2022a, *MNRAS*, **509**, 4256
 García-Bernete I., et al., 2022b, *A&A*, **666**, L5
 García-Bernete I., et al., 2024, *A&A*, **691**, A162
 García-Burillo S., et al., 2014, *A&A*, **567**, A125
 García-Burillo S., et al., 2019, *A&A*, **632**, A61
 García-Burillo S., et al., 2021, *A&A*, **652**, A98
 García-Burillo S., et al., 2024, *A&A*, **689**, A347
 Gliozzi M., Williams J. K., Akylas A., Papadakis I. E., Shuvo O. I., Halavatkar A., Alt A., 2024, *MNRAS*, **528**, 3417
 Gofford J., Reeves J. N., McLaughlin D. E., Braito V., Turner T. J., Tombesi F., Cappi M., 2015, *MNRAS*, **451**, 4169
 González-Martín O., et al., 2025, *MNRAS*, **539**, 2158
 Haidar H., et al., 2024, *MNRAS*, **532**, 4645
 Haidar H., et al., 2026, *arXiv e-prints*, p. arXiv:2601.02865
 Heckman T. M., Best P. N., 2014, *ARA&A*, **52**, 589
 Hermosa Muñoz L., et al., 2024, *A&A*, **690**, A350
 Hönig S. F., 2019, *ApJ*, **884**, 171
 Hönig S. F., Kishimoto M., 2010, *A&A*, **523**, A27
 Hönig S. F., Kishimoto M., 2017, *ApJ*, **838**, L20
 Hönig S. F., Kishimoto M., Antonucci R., Marconi A., Prieto M. A., Tristram K., Weigelt G., 2012, *ApJ*, **755**, 149
 Hönig S. F., et al., 2013, *ApJ*, **771**, 87
 Isbell J. W., et al., 2022, *A&A*, **663**, A35
 Joblin C., Tielens A. G. G. M., Allamandola L. J., Geballe T. R., 1996, *ApJ*, **458**, 610
 Jones A. P., Fanciullo L., Köhler M., Verstraete L., Guillet V., Bocchio M., Ysard N., 2013, *A&A*, **558**, A62
 Juneau S., et al., 2022, *ApJ*, **925**, 203

- Kormendy J., Ho L. C., 2013, *ARA&A*, **51**, 511
- Labiano A., et al., 2016, in Peck A. B., Seaman R. L., Benn C. R., eds, Society of Photo-Optical Instrumentation Engineers (SPIE) Conference Series Vol. 9910, Observatory Operations: Strategies, Processes, and Systems VI. p. 99102W ([arXiv:1608.05312](https://arxiv.org/abs/1608.05312)), doi:10.1117/12.2232554
- Lai T. S. Y., et al., 2023, [arXiv e-prints](https://arxiv.org/abs/2307.15169), p. [arXiv:2307.15169](https://arxiv.org/abs/2307.15169)
- Lange K., Dominik C., Tielens A. G. G. M., 2025, *A&A*, **702**, A14
- Leach S., 1986, *Journal of Electron Spectroscopy and Related Phenomena*, **41**, 427
- Lebouteiller V., Brandl B., Bernard-Salas J., Devost D., Houck J. R., 2007, *ApJ*, **665**, 390
- Leftley J. H., Tristram K. R. W., Hönl S. F., Kishimoto M., Asmus D., Gandhi P., 2018, *ApJ*, **862**, 17
- Li A., 2020, *Nature Astronomy*, **4**, 339
- López-Gonzaga N., Jaffe W., Burtscher L., Tristram K. R. W., Meisenheimer K., 2014, *A&A*, **565**, A71
- López-Gonzaga N., Burtscher L., Tristram K. R. W., Meisenheimer K., Schartmann M., 2016, *A&A*, **591**, A47
- Lopez S., et al., 2025, [arXiv e-prints](https://arxiv.org/abs/2510.01314), p. [arXiv:2510.01314](https://arxiv.org/abs/2510.01314)
- Mehdipour M., et al., 2021, *A&A*, **652**, A150
- Micelotta E. R., Jones A. P., Tielens A. G. G. M., 2010, *A&A*, **510**, A36
- Morris S., Ward M., Whittle M., Wilson A. S., Taylor K., 1985, *MNRAS*, **216**, 193
- Neškova M., Sirocky M. M., Ivezić Ž., Elitzur M., 2008a, *ApJ*, **685**, 147
- Neškova M., Sirocky M. M., Nikutta R., Ivezić Ž., Elitzur M., 2008b, *ApJ*, **685**, 160
- O'Dowd M. J., et al., 2009, *ApJ*, **705**, 885
- Packham C., Radomski J. T., Roche P. F., Aitken D. K., Perlman E., Alonso-Herrero A., Colina L., Telesco C. M., 2005, *ApJ*, **618**, L17
- Pauzat F., Talbi D., Ellinger Y., 1999, *MNRAS*, **304**, 241
- Peeters E., Hony S., Van Kerckhoven C., Tielens A. G. G. M., Allamandola L. J., Hudgins D. M., Bauschlicher C. W., 2002, *A&A*, **390**, 1089
- Pendleton Y. J., Allamandola L. J., 2002, *ApJS*, **138**, 75
- Pereira-Santaella M., et al., 2022, [arXiv e-prints](https://arxiv.org/abs/2208.04835), p. [arXiv:2208.04835](https://arxiv.org/abs/2208.04835)
- Pereira-Santaella M., et al., 2024, [arXiv e-prints](https://arxiv.org/abs/2404.16641), p. [arXiv:2404.16641](https://arxiv.org/abs/2404.16641)
- Phan D., Pradhan N., Jankowiak M., 2019, [arXiv e-prints](https://arxiv.org/abs/1912.11554), p. [arXiv:1912.11554](https://arxiv.org/abs/1912.11554)
- Poitevineau R., et al., 2025, *A&A*, **693**, A311
- Ponti G., Papadakis I., Bianchi S., Guainazzi M., Matt G., Uttley P., Bonilla N. F., 2012, *A&A*, **542**, A83
- Raban D., Jaffe W., Röttgering H., Meisenheimer K., Tristram K. R. W., 2009, *MNRAS*, **394**, 1325
- Radomski J. T., Piña R. K., Packham C., Telesco C. M., Tadhunter C. N., 2002, *ApJ*, **566**, 675
- Radomski J. T., et al., 2008, *ApJ*, **681**, 141
- Ramos Almeida C., Ricci C., 2017, *Nature Astronomy*, **1**, 679
- Ramos Almeida C., et al., 2025a, [arXiv e-prints](https://arxiv.org/abs/2512.02629), p. [arXiv:2512.02629](https://arxiv.org/abs/2512.02629)
- Ramos Almeida C., et al., 2025b, *A&A*, **698**, A194
- Rapacioli M., Calvo F., Joblin C., Parneix P., Toubanc D., Spiegelman F., 2006, *A&A*, **460**, 519
- Regan M. W., et al., 2006, *ApJ*, **652**, 1112
- Reunanen J., Prieto M. A., Siebenmorgen R., 2010, *MNRAS*, **402**, 879
- Ricci C., et al., 2017, *Nature*, **549**, 488
- Ricci T. V., Steiner J. E., May D., Garcia-Rissmann A., Menezes R. B., 2018, *MNRAS*, **473**, 5334
- Rigopoulou D., et al., 2021, *MNRAS*, **504**, 5287
- Rigopoulou D., et al., 2024, *MNRAS*, **532**, 1598
- Schnorr-Müller A., Storch-Bergmann T., Robinson A., Lena D., Nagar N. M., 2016, *MNRAS*, **457**, 972
- Schommer R. A., Caldwell N., Wilson A. S., Baldwin J. A., Phillips M. M., Williams T. B., Turtle A. J., 1988, *ApJ*, **324**, 154
- Schweitzer M., et al., 2006, *ApJ*, **649**, 79
- Shannon M. J., Boersma C., 2019, *ApJ*, **871**, 124
- Shimizu T. T., et al., 2019, *MNRAS*, **490**, 5860
- Shivaei I., Boogaard L. A., 2024, *A&A*, **691**, L2
- Silk J., Rees M. J., 1998, *A&A*, **331**, L1
- Smajić S., Fischer S., Zuther J., Eckart A., 2012, *A&A*, **544**, A105
- Stalevski M., Ricci C., Ueda Y., Lira P., Fritz J., Baes M., 2016, *MNRAS*, **458**, 2288
- Stalevski M., Asmus D., Tristram K. R. W., 2017, *MNRAS*, **472**, 3854
- Steiner J. E., Menezes R. B., Ricci T. V., Oliveira A. S., 2009, *MNRAS*, **395**, 64
- Sturm E., Lutz D., Verma A., Netzer H., Sternberg A., Moorwood A. F. M., Oliva E., Genzel R., 2002, *A&A*, **393**, 821
- Thatte N., et al., 2026, *MNRAS*, **545**, staf2047
- Tielens A. G. G. M., 2008, *ARA&A*, **46**, 289
- Tristram K. R. W., Burtscher L., Jaffe W., Meisenheimer K., Hönl S. F., Kishimoto M., Schartmann M., Weigelt G., 2014, *A&A*, **563**, A82
- Veenema O., et al. submitted 2026
- Veenema O., et al., 2025, *MNRAS*, **544**, 3361
- Venanzi M., Hönl S., Williamson D., 2020, *ApJ*, **900**, 174
- Villanueva V., et al., 2025, *A&A*, **695**, A202
- Viti S., et al., 2014, *A&A*, **570**, A28
- Voit G. M., 1992, *MNRAS*, **258**, 841
- Wada K., 2012, *ApJ*, **758**, 66
- Wexler A., 1967, *Applied Spectroscopy Reviews*, **1**, 29
- Wold M., Lacy M., Käufel H. U., Siebenmorgen R., 2006, *A&A*, **460**, 449
- Yang X. J., Li A., 2023, *ApJS*, **268**, 12
- Yang X. J., Glaser R., Li A., Zhong J. X., 2016, *MNRAS*, **462**, 1551
- Zhang L., et al., 2024a, *ApJ*, **974**, 195
- Zhang L., et al., 2024b, *ApJ*, **975**, L2
- Zhen J., Castellanos P., Paardekooper D. M., Ligterink N., Linnartz H., Nahon L., Joblin C., Tielens A. G. G. M., 2015, *ApJ*, **804**, L7

¹Department of Physics, University of Oxford, Keble Road, Oxford, OX1 3RH, UK

²Department of Astrophysics, University of California San Diego, 9500 Gilman Drive, San Diego, CA 92093, USA

³Centro de Astrobiología (CAB), CSIC-INTA, Camino Bajo del Castillo s/n, E-28692 Villanueva de la Cañada, Madrid, Spain

⁴School of Sciences, European University Cyprus, Diogenes Street, Engomi, 1516 Nicosia, Cyprus

⁵Instituto de Astrofísica de Canarias, Calle Vía Láctea, s/n, E-38205, La Laguna, Tenerife, Spain

⁶Departamento de Astrofísica, Universidad de La Laguna, E-38206, La Laguna, Tenerife, Spain

⁷Departamento de Física de la Tierra y Astrofísica, Fac. de CC. Físicas, Universidad Complutense de Madrid, 28040 Madrid, Spain

⁸Instituto de Física de Partículas y del Cosmos IPARCOS, Fac. CC. Físicas, Universidad Complutense de Madrid, 28040 Madrid, Spain

⁹School of Mathematics, Statistics and Physics, Newcastle University, Newcastle upon Tyne NE1 7RU, UK

¹⁰LUX, Observatoire de Paris, Collège de France, PSL University, CNRS, Sorbonne University, Paris, France

¹¹Max Planck Institute for Extraterrestrial Physics (MPE), Giessenbachstr. 1, 85748 Garching, Germany

¹²Institute of Astrophysics, Foundation for Research and Technology-Hellas (FORTH), Heraklion, GR-70013, Greece

¹³Centro de Estudios de Física del Cosmos de Aragón (CEFCA), Plaza San Juan 1, E-44001 Teruel, Spain

¹⁴Department of Physics & Astronomy, University of Southampton, Highfield, Southampton, SO17 1BJ, UK

¹⁵Observatorio Astronómico Nacional (OAN-IGN), Observatorio de Madrid, Alfonso XII, 3, 28014 Madrid, Spain

¹⁶Instituto de Radioastronomía y Astrofísica (IRyA), Universidad Nacional Autónoma de México, Morelia, Michoacán, Mexico

¹⁷Department of Physics & Astronomy, University of Alaska

Anchorage, Anchorage, AK 99508-4664, USA

¹⁸National Astronomical Observatory of Japan, National Institutes of Natural Sciences (NINS), 2-21-1 Osawa, Mitaka, Tokyo 181-8588, Japan

¹⁹Department of Astronomy, School of Science, Graduate University for Advanced Studies (SOKENDAI), Mitaka, Tokyo 181-8588, Japan

²⁰Telespazio UK for ESA, ESAC, Camino Bajo del Castillo s/n, 28692 Villanueva de la Cañada, Spain

²¹Space Telescope Science Institute, 3700 San Martin Drive, Baltimore, MD 21218, USA

²²Instituto de Física Fundamental, CSIC, Calle Serrano 123, 28006 Madrid, Spain

²³Department of Astronomy, University of Geneva, ch. d'Ecogia 16, 1290, Versoix, Switzerland

²⁴Instituto de Estudios Astrofísicos, Facultad de Ingeniería y Ciencias, Universidad Diego Portales, Av. Ejército Libertador 441, Santiago, Chile

²⁵Departamento de Física, CCNE, Universidade Federal de Santa Maria, Av. Roraima 1000, 97105-900 Santa Maria, RS, Brazil

²⁶LESIA, Observatoire de Paris, PSL Research University, CNRS, Sorbonne Université, Paris-Cité University, Meudon, France

²⁷Astronomical Observatory, Volgina 7, 11060 Belgrade, Serbia

²⁸Sterrenkundig Observatorium, Universiteit Gent, Krijgslaan 281-S9, B-9000 Gent, Belgium

²⁹Department of Physics and Astronomy, The University of Texas at San Antonio (UTSA), 1 UTSA Circle, San Antonio, TX 78249-0600, USA

APPENDIX A: SPECTRA

We show integrated spectra of all the Seyfert galaxies analysed in this work in Fig. A1. We extracted the spectra through a circular aperture with a radius of 2'' and thus the spectra contain contribution from both the AGN and the circumnuclear environment.

This paper has been typeset from a $\text{\TeX}/\text{\LaTeX}$ file prepared by the author.

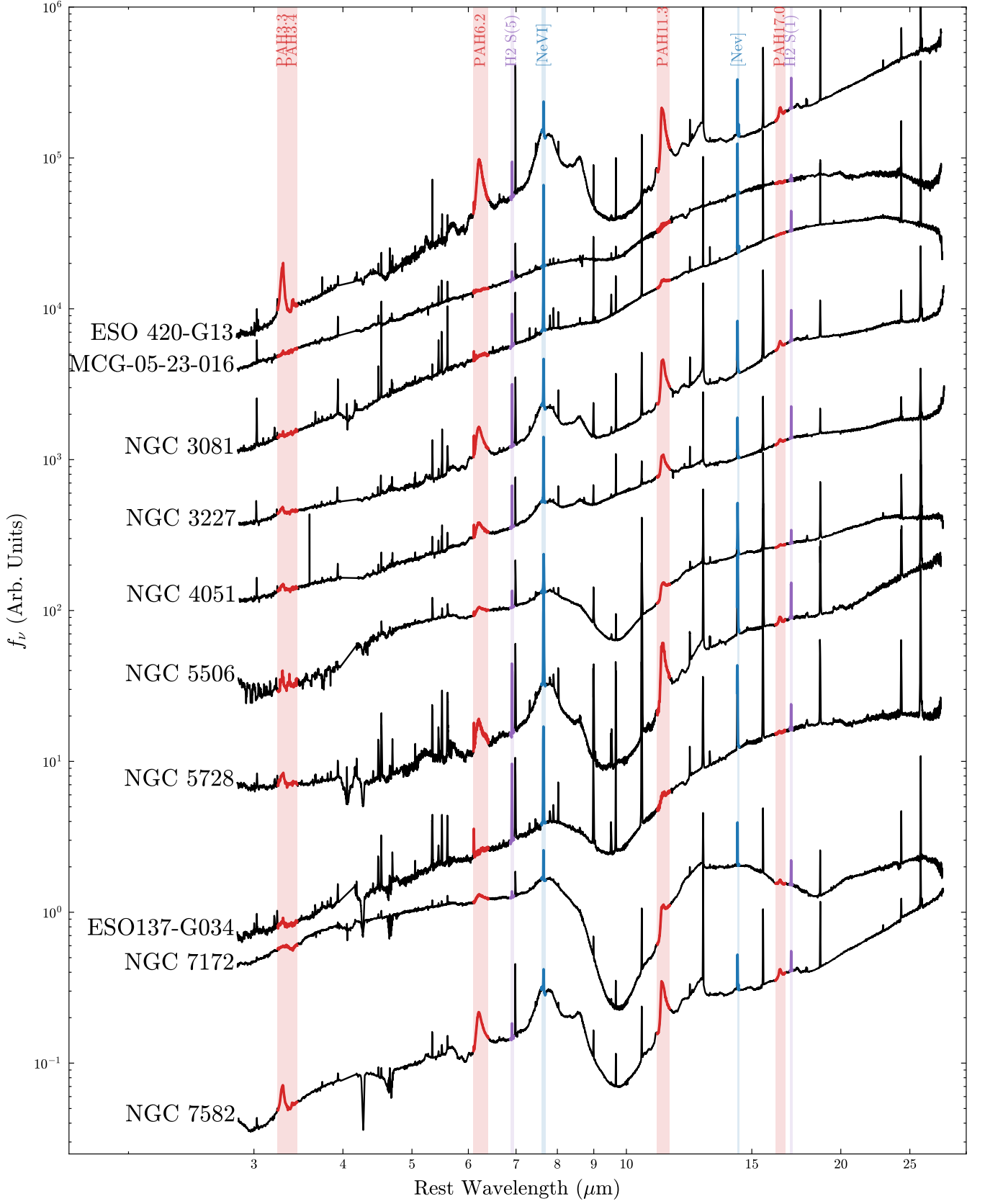


Figure A1. Integrated spectra of all 10 Seyfert galaxies used in this work, extracted from the NIRSpc and MIRI cubes through a wide, $2''$ radius aperture. We highlight the emission features used to create velocity maps with the PAHs in red, ionised gas in blue and molecular gas in purple. The spectra have been arbitrarily multiplicatively scaled in flux to make it easy to visualise.